

Reactivity of Chemisorbed Oxygen Atoms and Their Catalytic Consequences during CH₄–O₂ Catalysis on Supported Pt Clusters

Ya-Huei (Cathy) Chin,[†] Corneliu Buda,[‡] Matthew Neurock,^{‡,*} and Enrique Iglesia^{*,†}

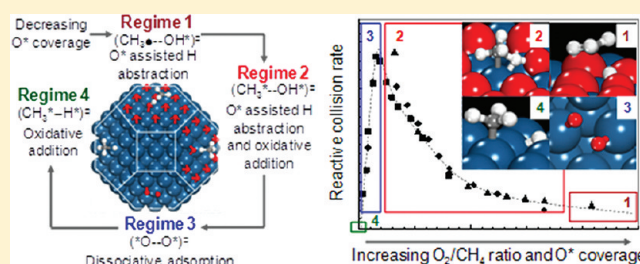
[†]Department of Chemical and Biomolecular Engineering, University of California, Berkeley, California 94720, United States

[‡]Departments of Chemical Engineering and Chemistry, University of Virginia, Charlottesville, Virginia 22904, United States

S Supporting Information

ABSTRACT: Kinetic and isotopic data and density functional theory treatments provide evidence for the elementary steps and the active site requirements involved in the four distinct kinetic regimes observed during CH₄ oxidation reactions using O₂, H₂O, or CO₂ as oxidants on Pt clusters. These four regimes exhibit distinct rate equations because of the involvement of different kinetically relevant steps, predominant adsorbed species, and rate and equilibrium constants for different elementary steps. Transitions among regimes occur as chemisorbed oxygen (O*) coverages change on Pt clusters. O* coverages are given, in turn, by a virtual O₂ pressure,

which represents the pressure that would give the prevalent steady-state O* coverages if their adsorption–desorption equilibrium was maintained. The virtual O₂ pressure acts as a surrogate for oxygen chemical potentials at catalytic surfaces and reflects the kinetic coupling between C–H and O=O activation steps. O* coverages and virtual pressures depend on O₂ pressure when O₂ activation is equilibrated and on O₂/CH₄ ratios when this step becomes irreversible as a result of fast scavenging of O* by CH₄-derived intermediates. In three of these kinetic regimes, C–H bond activation is the sole kinetically relevant step, but occurs on different active sites, which evolve from oxygen–oxygen (O*–O*), to oxygen–oxygen vacancy (O*–*), and to vacancy–vacancy (*–*) site pairs as O* coverages decrease. On O*-saturated cluster surfaces, O*–O* site pairs activate C–H bonds in CH₄ via homolytic hydrogen abstraction steps that form CH₃ groups with significant radical character and weak interactions with the surface at the transition state. In this regime, rates depend linearly on CH₄ pressure but are independent of O₂ pressure. The observed normal CH₄/CD₄ kinetic isotope effects are consistent with the kinetic-relevance of C–H bond activation; identical ¹⁶O₂–¹⁸O₂ isotopic exchange rates in the presence or absence of CH₄ show that O₂ activation steps are quasi-equilibrated during catalysis. Measured and DFT-derived C–H bond activation barriers are large, because of the weak stabilization of the CH₃ fragments at transition states, but are compensated by the high entropy of these radical-like species. Turnover rates in this regime decrease with increasing Pt dispersion, because low-coordination exposed Pt atoms on small clusters bind O* more strongly than those that reside at low-index facets on large clusters, thus making O* less effective in H-abstraction. As vacancies (*, also exposed Pt atoms) become available on O*-covered surfaces, O*–* site pairs activate C–H bonds via concerted oxidative addition and H-abstraction in transition states effectively stabilized by CH₃ interactions with the vacancies, which lead to much higher turnover rates than on O*–O* pairs. In this regime, O₂ activation becomes irreversible, because fast C–H bond activation steps scavenge O* as it forms. Thus, O* coverages are set by the prevalent O₂/CH₄ ratios instead of the O₂ pressures. CH₄/CD₄ kinetic isotope effects are much larger for turnovers mediated by O*–* than by O*–O* site pairs, because C–H (and C–D) activation steps are required to form the * sites involved in C–H bond activation. Turnover rates for CH₄–O₂ reactions mediated by O*–* pairs decrease with increasing Pt dispersion, as in the case of O*–O* active structures, because stronger O* binding on small clusters leads not only to less reactive O* atoms, but also to lower vacancy concentrations at cluster surfaces. As O₂/CH₄ ratios and O* coverages become smaller, O₂ activation on bare Pt clusters becomes the sole kinetically relevant step; turnover rates are proportional to O₂ pressures and independent of CH₄ pressure and no CH₄/CD₄ kinetic isotope effects are observed. In this regime, turnover rates become nearly independent of Pt dispersion, because the O₂ activation step is essentially barrierless. In the absence of O₂, alternate weaker oxidants, such as H₂O or CO₂, lead to a final kinetic regime in which C–H bond dissociation on *–* pairs at bare cluster surfaces limit CH₄ conversion rates. Rates become first-order in CH₄ and independent of coreactant and normal CH₄/CD₄ kinetic isotope effects are observed. In this case, turnover rates increase with increasing dispersion, because low-coordination Pt atoms stabilize the C–H bond activation transition states more effectively via stronger binding to CH₃ and H fragments. These findings and their mechanistic interpretations are consistent with all rate and isotopic data and with theoretical estimates of activation barriers and of cluster size effects on transition states. They serve to demonstrate the essential role of the coverage and reactivity of chemisorbed oxygen in determining the type and effectiveness of surface structures in CH₄ oxidation reactions using O₂, H₂O, or CO₂ as oxidants, as well as the diversity of rate dependencies, activation energies and entropies, and cluster size effects that prevail in these reactions. These results also show how theory and experiments can unravel complex surface chemistries on realistic catalysts under practical conditions and provide through the resulting mechanistic insights specific predictions for the effects of cluster size and surface coordination on turnover rates, the trends and magnitude of which depend sensitively on the nature of the predominant adsorbed intermediates and the kinetically relevant steps.



Received: March 16, 2011

Published: September 15, 2011

1. INTRODUCTION

The catalytic conversion of methane has been studied extensively because of its practical significance and apparent molecular simplicity.¹ Among chemical conversion routes, indirect conversion of CH₄ to H₂–CO mixtures using CO₂, H₂O, and/or O₂ oxidants remains the preferred route to fuels and chemicals from natural gas.^{2,3} Reforming processes use H₂O or CO₂ as coreactants and their endothermic nature ($\Delta H_{298}^0 = 206 \text{ kJ mol}^{-1}$ (H₂O), 247 kJ mol^{-1} (CO₂))³ and thermodynamic constraints lead to complex and costly infrastructure.⁴ CO₂ and H₂O reforming reactions proceed via the same catalytic sequence on all Group VIII metals (Ni,⁵ Rh,⁶ Pt,⁷ Ir,^{8,9} Ru,¹⁰ and Pd¹¹). The elementary steps involve activation of the first C–H bond in CH₄ as the sole kinetically relevant step. This step is kinetically coupled with sequential reactions of CH_x* species with oxygen atoms derived from CO₂ or H₂O in quasi-equilibrated steps on all metals except Pd.¹¹ The equilibrated steps of coreactant activation lead to CO₂/CO and H₂O/H₂ product ratios controlled exclusively by the thermodynamics of water-gas-shift reactions.

Catalytic partial oxidation (CPOX) uses O₂ for the selective conversion of CH₄ to CO and H₂ on metals^{12,13} (e.g., Pt, Ru, Ni) and oxides (e.g., La–Ru oxides) at moderate temperatures (1000–1200 K).^{14,15} This reaction is nearly thermoneutral ($\Delta H_{298}^0 = -38 \text{ kJ mol}^{-1}$) and avoids the extensive heat transfer and second-law inefficiencies inherent in reforming processes by coupling of exothermic and endothermic reactions at the molecular scale.¹⁶ CPOX maintains the stoichiometry and overall enthalpy achieved in practice through autothermal reforming,¹⁹ a process in which a flame at the reactor inlet uses O₂ to form H₂O and CO₂ and the heat released is used to convert residual CH₄ via catalytic reforming reactions. The relative rates of CH₄–O₂ and CH₄–H₂O/CO₂ reactions, the role of chemisorbed oxygen, and their catalytic consequences have remained inconclusive, even after considerable study. Short adiabatic catalytic reactors operating under extreme gradients in temperature and concentrations can form H₂ and CO with high selectivity, but claims for their direct formation from CH₄–O₂ reactants^{17,18} are inconsistent with other studies.^{19–21} These claims are also at odds with the exclusive formation of CO₂ and H₂O from CH₄–O₂ reactants before O₂ depletion,^{22,23} which indicate that combustion precedes reforming reactions and that partial oxidation does not occur at the molecular scale on catalyst surfaces.

These controversies reflect, at least in part, the thermal coupling of rapid combustion ($\Delta H_{298}^0 = -891 \text{ kJ mol}^{-1}$) and reforming reactions, which can occur within length scales of conductive and convective heat transports^{24,25} and lead to severe gradients across undiluted catalyst pellets and the reactor. Mechanistic interpretations of rate data are ubiquitously impaired by abrupt changes in oxygen surface coverages and most abundant surface intermediates and by metal–oxide phase transitions caused by concomitant changes in temperature and reactant concentrations within catalyst pellets and along the catalyst bed. Reported rate data under conditions of strict kinetic control and without transport artifacts show that CO₂ and H₂O are the nearly exclusive products of CH₄–O₂ reactions on Pt and Rh clusters at relevant O₂ pressures and that a trace amount of CO is detected only at O₂/CH₄ ratios below 0.04 (873 K).²⁶ Competitive reactions of ¹²CO and ¹³CH₄ with O₂ on Pt confirmed that any CO that desorbs would form CO₂ at rates much faster than the initial C–H bond activation step,²⁶ as also found on Rh²⁶ and Pd²⁷ catalysts. CO and H₂ formed only via sequential reforming reactions after O₂ depletion

and partial oxidation occurs in practice only by axial thermal coupling of combustion and reforming reactions on Pt, Rh, and Pd catalysts.

Here, we provide a rigorous mechanistic interpretation of CH₄–O₂ reactions on supported Pt clusters, based on kinetic and isotopic data obtained under conditions of strict kinetic control and results from density functional theory (DFT) calculations. We propose a sequence of elementary steps and describe how kinetically relevant steps and surface intermediates evolve as O₂ and CH₄ pressures change. The changes in the identities of the kinetically relevant steps and surface intermediates lead to four distinct kinetic regimes, each with a unique rate equation, cluster size dependence, and CH₄/CD₄ kinetic isotope effects. Transitions among regimes are delineated by the coverage of chemisorbed oxygen atoms (O*) on Pt cluster surfaces. In three of these regimes, C–H bond activation is the kinetically relevant step, but occurs on different active site structures of oxygen–oxygen (O*–O*), oxygen–vacancy (O*–*), or vacancy–vacancy (*–*) site pairs as the O* coverage decreases. At very low O₂/CH₄ ratios, C–H bond activation is kinetically irrelevant, as O₂ dissociation on bare Pt cluster surfaces becomes the sole kinetically relevant step. Transitions among the kinetic regimes are prescribed rigorously by oxygen chemical potentials at Pt cluster surfaces, which are set by the kinetic coupling of C–H and O=O bond activation steps and are shown here to depend on either the O₂ pressures or O₂/CH₄ ratios for quasi-equilibrated or irreversible O₂ activation, respectively.

2. METHODS

2.1. Catalyst Synthesis. γ -Al₂O₃ (Sasol North America Inc., lot number C1643, $193 \text{ m}^2 \text{ g}^{-1}$, $0.57 \text{ cm}^3 \text{ g}^{-1}$ pore volume) and SiO₂ (Davison Chemical, Chromatographic Silica Media, CAS no. 112926–00–8, lot number 995, $280 \text{ m}^2 \text{ g}^{-1}$, $0.85 \text{ cm}^3 \text{ g}^{-1}$ pore volume) were treated in flowing dry air (Praxair, 99.99%, $0.8 \text{ cm}^3 \text{ g}^{-1} \text{ s}^{-1}$) to 923 K for 3 h (0.083 K s^{-1} ramp). Pt catalysts were prepared by incipient wetness impregnation of γ -Al₂O₃ or SiO₂ with aqueous hexachloroplatinic acid (H₂PtCl₆·(H₂O)₆, Aldrich, CAS #16941–12–1). Samples were treated in ambient air at 383 K for >8 h and in flowing dry air (Praxair, 99.99%, $0.8 \text{ cm}^3 \text{ g}^{-1} \text{ s}^{-1}$) to 823 K (0.033 K s^{-1} ramp) for 3 h. Portions of the catalyst were then treated at temperatures between 900 and 1023 K (0.033 K s^{-1} ramp) in flowing dry air (Praxair, 99.99%, $0.8 \text{ cm}^3 \text{ g}^{-1} \text{ s}^{-1}$) for 5 h to vary the size of Pt clusters between 1.8 and 8.5 nm and then cooled to ambient temperature. These catalysts were finally treated at temperatures between 873 and 923 K in flowing 10% H₂/Ar (Praxair certified standard, 0.083 K s^{-1} ramp, $0.8 \text{ cm}^3 \text{ g}^{-1} \text{ s}^{-1}$) for 2 h, cooled to ambient temperature in flowing He (Praxair UHP grade), and then held in flowing 1% O₂/He (Praxair certified standard, $0.8 \text{ cm}^3 \text{ g}^{-1} \text{ s}^{-1}$) at ambient temperature for at least 4 h before exposure to ambient air. The mean cluster size in these samples was calculated from volumetric uptakes of chemisorbed hydrogen at 313 K, which were measured using a Quantasorb Analyzer (Quantachrome Corp.), extrapolated to zero pressure by assuming a 1:1 H/Pt_s (Pt_s denotes surface Pt atoms) adsorption stoichiometry, hemispherical clusters, and density of the Pt clusters similar to that of bulk Pt metal (21.5 g cm^{-3}).²⁸

2.2. Steady-State Catalytic Rate Measurements. CH₄ conversion turnover rates and selectivities were measured in a tubular flow reactor (quartz; 8.1 mm inner diameter) using catalyst particles diluted with silicon dioxide granules to prevent temperature gradients. Reaction temperatures (810–900 K) were measured with a K-type thermocouple held within a concentric quartz thermowell. The catalyst was mixed with SiO₂ (Davison Chemical, Chromatographic Silica Media, CAS no. 112926–00–8, $280 \text{ m}^2 \text{ g}^{-1}$; treated in flowing dry air; Praxair, 99.99%,

0.8 cm³ g⁻¹ s⁻¹, 0.083 K s⁻¹ ramp for 5 h at 1123 K) to achieve a 200 intraparticle diluent-to-catalyst ratio (λ). The physical mixtures were pelleted and sieved to retain agglomerates with 0.1–0.25 mm diameter. These pellets were further diluted with silicon dioxide granules (Fluka, acid purified, product number 84880; 0.1–0.25 mm diameter) to give a bed diluent-to-catalyst (Pt on Al₂O₃ or SiO₂) weight ratio (χ) of 4700. Both SiO₂ diluents did not lead to detectable CH₄–O₂ rates at any of the conditions of these experiments. The intra- and interparticle dilution ratios above were shown to avoid temperature and concentration gradients within catalyst pellets or bed and to ensure that rate and selectivity data reflect chemical reaction dynamics under conditions of strict kinetic control.²⁶

Catalyst mixtures that contain 0.15 mg of Pt/Al₂O₃ or Pt/SiO₂ were treated in situ in flowing H₂ (Praxair UHP grade, 0.083 K s⁻¹ ramp, 0.5 cm³ s⁻¹) at reaction temperatures (813–898 K) for 1 h and then in He (Praxair UHP grade, 2.1 cm³ s⁻¹) for 0.167 h before rate measurements. Mixed gases (Praxair certified standard, 25% CH₄/Ar, 5% O₂/He, 50% CO₂/N₂, and 1% CO/He) and O₂ (Praxair UHP grade) were used as reactants with He (Praxair UHP grade) as an inert diluent. Flow rates were metered with electronic flow controllers (Porter, type 201). Effects of H₂O on the reaction rates were probed by introducing distilled and deionized water into an evaporation volume held at 423 K, which allows mixing with the gaseous reactant stream, using a gas tight syringe (Hamilton #1005, 5000 μ L) and a syringe micropump (Cole Parmer, model 60061). CO₂, CH₄, and CO concentrations were measured by gas chromatography (Agilent 3000A) equipped with Poraplot Q and Molecular Sieve 5A columns connected to thermal conductivity detectors. CH₄ conversion rates are reported based on CO and CO₂ concentrations in the effluent stream and confirmed from residual CH₄ concentrations in an experiment of high CH₄ conversions (>20%). Kinetic measurements and the rate data reported herein were carried out at less than 5% CH₄ conversions.

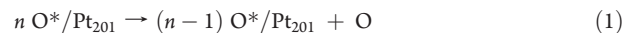
CD₄-O₂, CH₄-CD₄-O₂, ¹³CH₄-CO₂-O₂, CH₄-¹⁶O₂-¹⁸O₂, and ¹⁶O₂-¹⁸O₂ reactant mixtures were prepared with ¹³CH₄ (Isotec, chemical purity >99.0%), CD₄ (Isotec, chemical purity >99.0%), or 2% ¹⁸O₂/He mixture (Icon, 98% isotopic purity) in addition to the reactant gases. Kinetic isotope effects and exchange rate measurements were carried out using methods similar to those described above. The concentrations of CH₄, CO₂, and O₂ isotopologues (CH_xD_y, (x + y = 4), ¹³C¹⁶O₂, ¹²C¹⁶O₂, ¹²C¹⁶O¹⁸O, ¹²C¹⁸O₂, ¹⁸O₂, ¹⁶O₂, ¹⁶O¹⁸O) were measured with a mass selective detector (Agilent 5973). Catalysts were treated in CH₄-¹⁶O₂-¹⁸O₂ mixtures before the oxygen exchange rate measurements in ¹⁶O₂-¹⁸O₂ and in CH₄-¹⁶O₂-¹⁸O₂ mixtures. During the pretreatment, oxygen atoms in C¹⁶O₂, C¹⁸O₂, and C¹⁶O¹⁸O isotopologues formed from CH₄-¹⁶O₂-¹⁸O₂ reactions also exchanged with the lattice oxygen (O_L^{*}) in Al₂O₃ support. The rapid exchange between CO₂ isotopologues and O_L^{*} in Al₂O₃ causes the ¹⁸O_L^{*} to ¹⁶O_L^{*} ratio on the Al₂O₃ support to become identical to the ratios of ¹⁸O₂(g)/¹⁶O₂(g) and of ¹⁸O^{*}/¹⁶O^{*} on Pt cluster surfaces. The oxygen exchange rate measurements were carried out after the isotopic contents of Al₂O₃ support and Pt clusters became identical, as confirmed by the distribution of CO₂ isotopologues in statistical ratios during the treatment in CH₄-¹⁶O₂-¹⁸O₂ mixtures. H₂O, D₂O, and HDO molecules formed in CH₄-CD₄-O₂ reactions were removed from the effluent stream with anhydrous CaSO₄ (Drierite) before mass spectrometric analysis. Pt/SiO₂ was used instead of Pt/Al₂O₃ samples to determine the CH₄-CD₄ cross exchange rates on Pt because Al₂O₃ supports also catalyze the CH₄-CD₄ cross exchange steps in CH₄-CD₄-O₂ mixtures.

2.3. Computational Methods. A number of studies previously reported in the literature have examined the adsorption and activation of CH₄ over different single crystal surfaces at low coverage conditions.^{29–42} The results from these studies indicate that the C–H bond of CH₄ is activated via an oxidative addition of the metal atom into the C–H bond that results in the formation of a three-centered transition state involving the metal, C, and H atoms. While these studies offer important insights

into the activation of C–H bonds, there are very few studies that examine the catalytic consequences of oxygen atoms, except for studies of C–H bond activation in CH₄²⁶ on O^{*} covered Pt clusters and on closed-packed Pd, Rh, Au, Ag, and Cu surfaces,⁴³ and in CH₃OCH₃ on O^{*} covered Pt(111).⁴⁴ Herein, we carry out nonlocal gradient-corrected periodic plane wave density functional theory (DFT) calculations as implemented in the Vienna Ab-Initio Simulations Package (VASP)^{45–47} to determine the adsorption energies for oxygen and CH₄ as well as the activation barriers and energies for CH₄ and oxygen reactions over model 1.8 nm cuboctahedral Pt clusters. All calculations discussed herein were carried out using the Perdew–Wang 91 (PW91)⁴⁸ form of the generalized gradient approximation (GGA) to determine the corrections to the exchange and correlation energies. The wave functions used to describe the system were represented by a periodic expansion of plane-waves with a basis set cutoff energy of 38 214 kJ mol⁻¹ (396 eV) where the interactions between core and valence electrons were described by Vanderbilt ultrasoft pseudopotentials (US-PP).⁴⁹ The electronic energies for all structures were converged to within 9.65 × 10⁻³ kJ mol⁻¹ (1 × 10⁻⁴ eV). The geometric structures were all optimized until the forces on each atom were within 48.25 kJ (mol nm)⁻¹ (0.5 eV nm⁻¹).

The model 1.8 nm Pt cluster used to carry out the simulations consisted of 201 Pt atoms arranged in a cuboctahedral structure containing eight (111) and six (100) edge-sharing facets (Scheme 1), as described previously⁵⁰ and denoted herein as Pt₂₀₁. The cluster contains four types of Pt atoms (sites 1–4), depending on their coordination numbers, and five distinct types of O^{*} adsorption sites (sites I–V) on the (111) and (100) facets. The cluster was placed at the center of a 3 × 3 × 3 nm³ unit cell with a minimum distance of 0.8 nm from the edges of the cell, the details of which are provided elsewhere.²⁶ A (1 × 1 × 1) Monkhorst-Pack *k*-point mesh⁵¹ grid (unshifted) was used to sample the first Brillouin zone and calculate the total electronic energies of the Pt₂₀₁ systems. These energies were used to approximate the enthalpies for all systems considered here. The rigorous calculation of enthalpies would require accurate second-derivative calculations to determine energy changes with respect to all nuclear degrees of freedom to obtain vibrational frequencies and zero-point energies and accurate assessments of the rotational and translational energies. Such calculations would require unrealistic supercomputing CPU resources and would only influence the calculated reaction energies by less than 15 kJ mol⁻¹.

O^{*} saturation on Pt₂₀₁ clusters (1 ML O^{*} coverage) is achieved by placing oxygen atoms in each threefold fcc site on (111) facets and each twofold bridge site on (100) facets. Coverage is defined as the O^{*}/O^{*}_{max} ratio, where O^{*}_{max} is the number of O^{*} at saturation coverages. The O^{*} binding strength was defined as the absolute value of reaction energy required to remove an O^{*} atom on O^{*} covered Pt clusters:

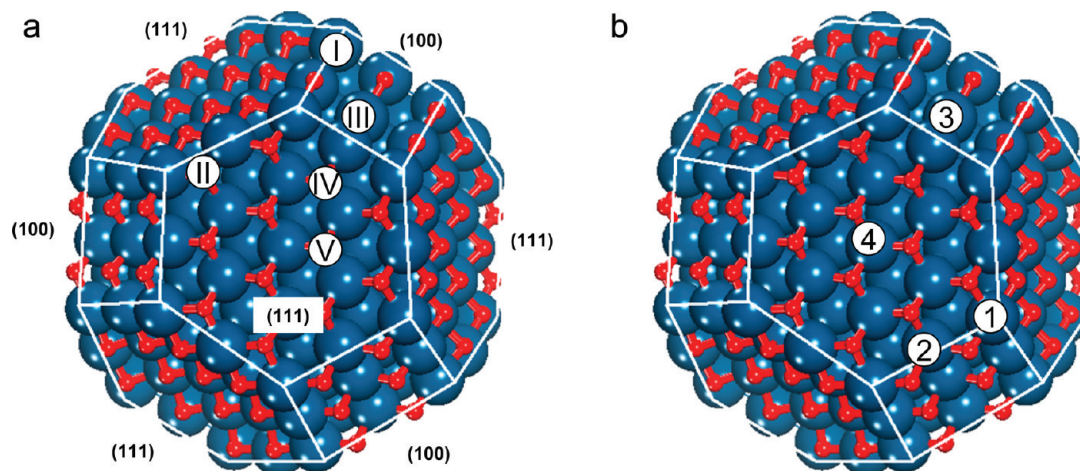


where the $n \text{ O}^*/\text{Pt}_{201}$ and $(n - 1) \text{ O}^*/\text{Pt}_{201}$ are in their optimized structures.

All activation barriers were calculated using the climbing image-nudged elastic band (CI-NEB) methods to locate transition states.^{52–54} This method first minimizes the forces normal to the reaction trajectory on all of the atoms in evolving structures initially chosen at equally spaced points along the reaction coordinate to within 48.2 kJ (mol nm)⁻¹ (0.5 eV nm⁻¹). The climbing algorithm is then used to maximize the energy of the climbing image along the reaction coordinate while minimizing the energy in all other directions. The transition states reported here were converged to structures for which the forces on all of the atoms were < 48.2 kJ (mol nm)⁻¹ (0.5 eV nm⁻¹). The barriers are referenced with respect to gaseous reactant molecules to compare them with measured activation energies.

3. RESULTS AND DISCUSSION

3.1. Kinetic Dependence and Selectivity of CH₄–O₂ Reactions. Rate data were measured at intraparticle (λ) and bed (χ)

Scheme 1^a

^a(a,b) A 201 atom cuboctahedral Pt cluster (1.8 nm cluster diameter) consists of eight (111) and six (100) facets that are saturated with chemisorbed O* atoms. There are five distinct types of O* atoms (labeled I–V) and four types of Pt atoms (labeled 1–4) on the facets. O* atoms chemisorb on threefold fcc sites on the (111) (types II, IV, and V) and twofold bridge sites on the (100) (types I and III) facets. Saturation occurs at full coverage in which all of the sites I–V on the cluster are occupied by O* atoms.

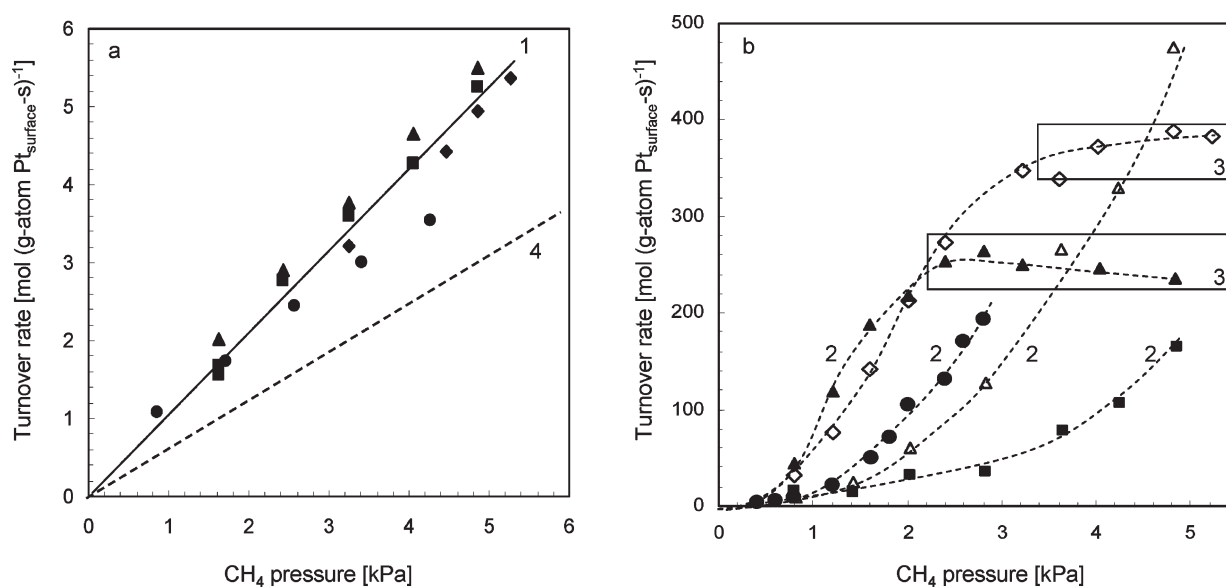


Figure 1. (a) CH₄ turnover rates (873 K) during CH₄–O₂ reactions at 8.1 kPa (■) and 22.7 kPa (▲) O₂ and during ¹³CH₄–O₂–CO₂ (◆) and CH₄–O₂–H₂O (●) reactions (22.7 kPa O₂, 5 kPa CO₂ or H₂O) in regime 1 (labeled as 1, O₂/CH₄ > 2) on Pt clusters (8.5 nm average cluster size) plotted against the CH₄ pressure. CH₄ reforming rates (regime 4, labeled as 4, without O₂) are extrapolated using the rate constant (reported in ref 7) and shown here for comparison (1: regime 1, O₂/CH₄ > 2; 4: regime 4, O₂/CH₄ = 0). (b) CH₄ turnover rates (873 K) during CH₄–O₂ reactions on Pt clusters (8.5 nm average cluster size) for O₂ pressures of 0.17 kPa (▲), 0.27 kPa (◇), 0.39 kPa (●), 0.70 kPa (Δ), 1.6 kPa (■), as a function of CH₄ pressure for O₂/CH₄ ratios between 0.035 and 2. These rate data measured in regimes 2 and 3 (as defined by the O₂/CH₄ ratio) are labeled as 2 and 3, respectively. (2: regime 2, 0.08 < O₂/CH₄ < 2; 3: regime 3, 0 < O₂/CH₄ < 0.08). (0.15 mg 0.2% wt Pt/Al₂O₃, 200 SiO₂/catalyst intraparticle (λ) and 4700 quartz/catalyst interparticle dilution (χ) ratios, 2.08 cm³ (STP) s⁻¹).

dilution ratios ($\lambda = 200$; $\chi = 4700$) larger than those required to avoid temperature and concentration gradients, confirmed from measured rates, and selectivities remained unchanged upon further dilution.²⁶ Turnover rates were independent of the ratio of void volume to catalyst mass in reactors, consistent with the absence of homogeneous reactions. Thus, all reported reaction rates reflect the intrinsic dynamics of chemical events at catalytic surfaces unaffected by transport artifacts or gas phase reactions.

Figures 1 and 2 show CH₄ turnover rates (denoted as rates herein, per surface Pt atom; 873 K, 0.2% wt Pt/Al₂O₃, 8.5 nm average cluster diameter) as a function of CH₄ (0.4–4.9 kPa) and O₂ (0–23.0 kPa) pressures, respectively. Four kinetic regimes (labeled 1–4 in the figures) are evident from these data; each regime exhibits different rate equations and CH₄/CD₄ kinetic isotope effects (sections 3.2–3.4). CO was not detected in regime 1 or 2 and formed only in trace amounts (CO/CO₂ < 0.005) at the

lowest O_2 pressures ($O_2/CH_4 < 0.08$) in regime 3. These data show that CH_4 reacts predominantly via combustion reactions at all relevant O_2/CH_4 ratios and that CO selectivities become detectable only after O_2 depletion or when H_2O or CO_2 are used as coreactants (regime 4);²⁶ in the latter case, the effluent CO/ CO_2 ratios correspond to those expected from water-gas-shift equilibrium.⁷

Rates at 873 K depend linearly on CH_4 pressure but are not influenced by O_2 pressure for O_2/CH_4 ratios between 2.0 and 4.6 (regime 1, labeled 1, Figure 1a), which are typical of catalytic combustion practice. At lower O_2/CH_4 ratios ($0.08 < O_2/CH_4 < 2$), rates (r_2) show a stronger than linear dependence on CH_4 pressure and increase with decreasing O_2 pressure (regime 2, 2 in Figure 1b) in a

manner accurately described by the rate equation

$$r_2 = k_{\text{eff},2} \frac{(CH_4)^2}{(O_2)} \quad (2)$$

where $k_{\text{eff},2}$ denotes an apparent rate constant. For O_2/CH_4 ratios below 0.08 (regime 3, 3 in Figure 1b), rates become independent of CH_4 pressure and proportional to O_2 pressure. These kinetic regimes are also evident from the effects of O_2 pressure on rates at each CH_4 pressure (Figure 2) and from the measured effects of increasing residence time,²⁶ which causes a concomitant decrease in O_2/CH_4 ratios along the catalyst bed.

H_2O (5 kPa) or CO_2 (5 kPa) in CH_4-O_2 (or $^{13}CH_4-O_2$) reactants did not influence turnover rates (Figures 1a and 2) for any of these regimes, even when O_2 was excluded from the stream and H_2O or CO_2 were the only coreactants (regime 4, 4 in Figure 1a).⁷ Thus, H_2O and CO_2 do not modify the coverages of reactive intermediates and active site structures during CH_4 reactions with O_2 , H_2O , or CO_2 in all regimes. They also do not catalyze the reforming reactions at detectable rates when O_2 is present.

Pseudo first-order rate constants ($r_{CH_4}(CH_4)^{-1}$), determined from the rate data in Figures 1 and 2, are a single-valued function of O_2/CH_4 ratios (Figure 3), irrespective of the individual CH_4 and O_2 pressures. At high O_2/CH_4 ratios (>2 , regime 1), $r_{CH_4}(CH_4)^{-1}$ values do not depend on O_2 pressure and rigorously represent the reactive collision probabilities of CH_4 . As O_2/CH_4 ratios decrease to between 0.08 and 2 (regime 2), $r_{CH_4}(CH_4)^{-1}$ become inversely proportional to O_2/CH_4 ratios. A further decrease in O_2/CH_4 ratio (<0.08 , regime 3) leads to $r_{CH_4}(CH_4)^{-1}$ proportional to O_2/CH_4 ratios, indicating that turnover rates depend linearly on O_2 pressure.

A sequence of elementary steps is proposed in Scheme 2, which includes elementary steps that form CO_2 , H_2O , CO , and H_2 . The latter two species may form via desorption of their respective adsorbed precursors (CO^* and H^*) before subsequent oxidation by O^* . C–H bonds in CH_4 are activated using chemisorbed oxygen–oxygen (O^*-O^*), oxygen–oxygen vacancy (O^*-*), or vacancy–vacancy ($*-*$) site pairs (Steps 1.1–1.3,

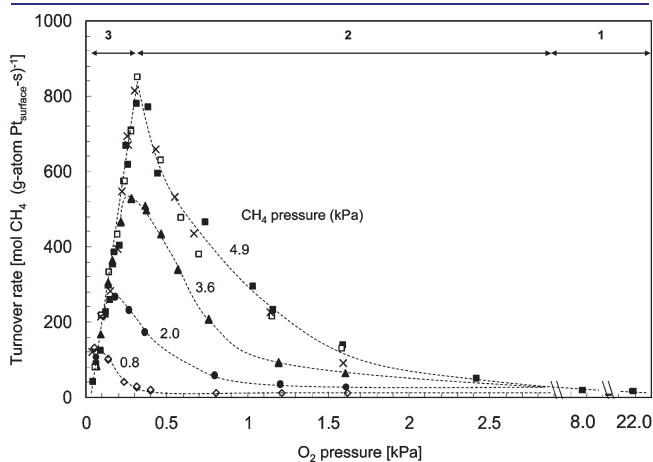


Figure 2. CH_4 turnover rates (873 K) during CH_4-O_2 reactions with 0.8 kPa (\diamond), 2.0 kPa (\bullet), 3.6 kPa (\blacktriangle), or 4.9 kPa (\blacksquare) CH_4 and during $^{13}CH_4-O_2-CO_2$ (\times) and $CH_4-O_2-H_2O$ (\square) reactions with either 5 kPa CO_2 or 5 kPa H_2O on Pt clusters (8.5 nm average cluster size) as a function of O_2 pressure. Kinetic regimes 1–3 are labeled 1–3, respectively. (0.15 mg 0.2% wt Pt/ Al_2O_3 , 200 SiO_2 /catalyst intraparticle (λ) and 4700 quartz/catalyst interparticle (χ) dilution ratios, 2.08 cm^3 (STP) s^{-1} ; 1: $O_2/CH_4 > 2$; 2: $0.08 < O_2/CH_4 < 2$; 3: $0 < O_2/CH_4 < 0.08$).

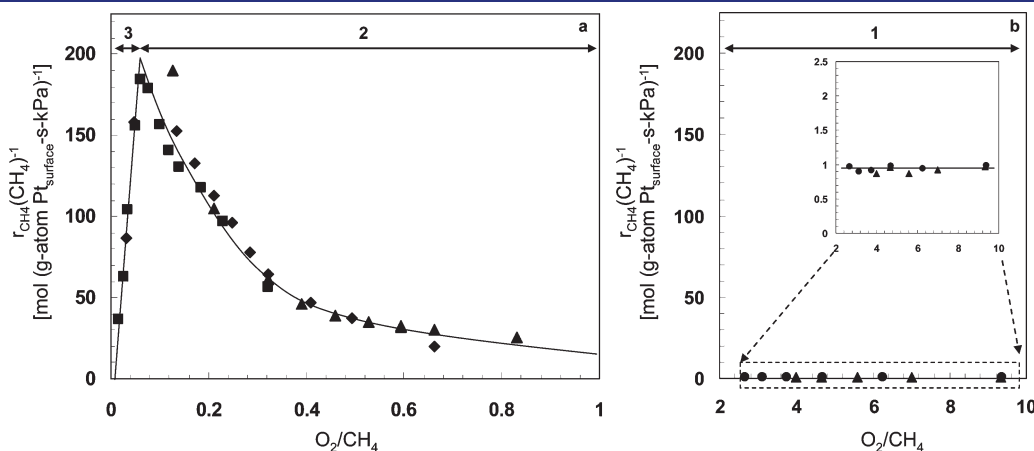


Figure 3. (a) Pseudo first-order rate constant ($r_{CH_4}(CH_4)^{-1}$) for CH_4-O_2 reactions as a single-valued function of O_2/CH_4 ratio on Pt clusters (8.5 nm average cluster size) with 1.2 kPa (\bullet), 2.4 kPa (\blacktriangle), and 4.8 kPa (\blacksquare) CH_4 in kinetic regimes 2 (labeled as 2, $0.08 < O_2/CH_4 < 2$) and 3 (labeled as 3, $0 < O_2/CH_4 < 0.08$). (b) Pseudo first-order rate constant ($r_{CH_4}(CH_4)^{-1}$) for CH_4-O_2 reactions as a single-valued function of O_2/CH_4 ratio on Pt clusters (8.5 nm average cluster size) with 8 kPa (\blacklozenge), 15 kPa (\bullet), and 22 kPa (\blacktriangle) O_2 in kinetic regime 1 (labeled as 1, $O_2/CH_4 > 2$). (0.15 mg 0.2% wt Pt/ Al_2O_3 , 873 K, 200 SiO_2 /catalyst intraparticle (λ) and 4700 quartz/catalyst interparticle (χ) dilution ratios, 2.08 cm^3 (STP) s^{-1}).

refer to Scheme 2 herein and after for the elementary steps) and O=O bonds are activated on $*-*$ site pairs in kinetically relevant steps that give rate equations, activation barriers, and activation entropies consistent with rate data in the four kinetic regimes (Table 1). Kinetically relevant steps and most abundant surface intermediates (MASI) depend only on O^* coverages, which are set, in turn, by either the O_2 pressures (regime 1) or the O_2/CH_4 reactant ratios (regimes 2 and 3) (to be discussed in sections 3.2–3.4).

In what follows, we show that these mechanism-based rate equations and kinetic parameters accurately describe all rate data

Scheme 2. Elementary Steps for CH_4-O_2 , CH_4-CO_2 , CH_4-H_2O , and $^{16}O_2-^{18}O_2$ Isotopic Oxygen Exchange Reactions^a

Step	Elementary reaction step	Rate and equilibrium constant
1.1	$CH_4 + O^* + O^* \longrightarrow CH_3O^* + OH^*$	$k_{1[O^*-O^*]}$
1.2	$CH_4 + O^* + * \longrightarrow CH_3^* + OH^*$	$k_{1[O^*-*]}$
1.3	$CH_4 + ** \longrightarrow CH_3^* + H^*$	$k_{1[*-*]}$
2.1	$O_2 + * \rightleftharpoons O_2^*$	k_{2af}, k_{2ar}
2.2	$O_2^* + * \rightleftharpoons 2O^*$	k_{2bf}, k_{2br}
3	$C^* + O^* \rightleftharpoons CO^* + *$	k_3
4	$CO^* + O^* \rightleftharpoons CO_2^* + *$	k_{4f}, k_{4r}
5	$2H^* \rightleftharpoons H_2 + 2^*$	K_{H_2}
6	$H^* + O^* \rightleftharpoons OH^* + *$	K_{O^*,H^*}
7	$CO_2^* \rightleftharpoons CO_2 + *$	K_{CO_2}
8	$2OH^* \rightleftharpoons H_2O^* + O^*$	K_{OH^*}
9	$H_2O^* \rightleftharpoons H_2O + *$	K_{H_2O}
10	$CO^* \rightleftharpoons CO + *$	K_{CO}
11 ^a	$^xO_2^* + ^yO^* \longrightarrow ^xO^* + ^yO^*$	k_{11f}, k_{11r}

^a x and y are used in this equation to differentiate the oxygen atoms. \longrightarrow denotes an irreversible step and \rightleftharpoons a quasi-equilibrated step; k_{if} and k_{ir} are the forward and reverse rate coefficients of step i , respectively, and K_i is the equilibrium constant for step i .

(Figures 1–3) and that assumptions about the kinetic relevance and reversibility of C–H and O=O activation steps are consistent with CH_4/CD_4 kinetic isotope effects (KIE) and CH_4-CD_4 and $^{16}O_2-^{18}O_2$ isotopic exchange rate data measured during CH_4-O_2 catalysis. Measured activation barriers and entropies for kinetically relevant steps are in agreement with density functional theory estimates as O^* coverages vary on Pt_{201} clusters. We report these results and simulations for each kinetic regime in the order of decreasing O^* coverages, starting with the kinetic, isotopic, and theoretical results in regime 1 ($O_2/CH_2 > 2$), for which the C–H bond activation on the O^*-O^* site pairs present on saturated Pt surfaces is the sole kinetically relevant step.

3.2. Kinetically-Relevant C–H Bond Activation on Pt Surfaces Saturated with Chemisorbed Oxygen. CH_4 turnover rates for CH_4-O_2 reactions in regime 1 ($O_2/CH_4 > 2$) are proportional to CH_4 pressure and independent of O_2 pressure (Figure 1). These results, together with CH_4/CD_4 KIE values larger than unity and independent of O_2 pressure (KIE = 1.66 at 873 K; $O_2/CH_4 > 2$), suggest that kinetically relevant C–H bond activation steps occur on surfaces containing species at coverages and reactivities that do not depend on O_2 pressure. Rates for CH_4 reactions with H_2O or CO_2 (regime 4) also depend similarly on the CH_4 and coreactant pressures.⁷ CH_4/CD_4 kinetic isotope effects in CH_4-H_2O/CO_2 mixtures are also larger than unity and independent of coreactant identity (KIE, 1.69 (H_2O) and 1.77 (CO_2), 873 K, Table 1) on Pt,⁷ as also found on other group VIII metals (1.66 (Ni),⁵ 1.54 (Rh),⁶ 1.81 (Ir),⁸ and 1.40 (Ru)¹⁰ for H_2O reforming, 873 K). Our previous results have shown that the CH_4-H_2O/CO_2 reactions proceed via C–H bond cleavage assisted by metal atom site pairs ($*-*$) on essentially bare cluster surfaces (Step 1.3, Scheme 2). Activation energies and pre-exponential factors for CH_4-H_2O/CO_2 (regime 4) and CH_4-O_2 (regime 1) reactions, however, differ significantly, as shown in Figure 4 and Table 1. These differences led us to conclude that kinetically relevant C–H bond activation steps in CH_4-O_2 mixtures occur on surfaces different from those in CH_4-H_2O/CO_2 mixtures; therefore the C–H bond activation steps in CH_4-O_2 mixtures occur over Pt cluster surfaces that are

Table 1. Rate Equations, Kinetically Relevant Steps, Kinetic Parameters, and Kinetic Isotope Effects for the Various Kinetic Regimes during CH_4-O_2 Reactions on 0.2% wt Pt/ Al_2O_3 Catalyst (8.5 nm average Pt cluster size)

kinetic regime and MASI ^d	rate equation	kinetically relevant step	effective rate constant ^b (k_{eff})	kinetic isotope effect ^c (873 K)	apparent activation energy (kJ mol ⁻¹)	pre-exponential factor (kPa ⁻¹ s ⁻¹)	entropy loss (J mol ⁻¹ K ⁻¹)
Regime 1 (O^*-O^*)	$k_{eff1}(CH_4)$	$CH_4 + O^* + O^* \xrightarrow{k_{1[O^*-O^*]}} CH_3O^* + OH^*$	$k_{1[O^*-O^*]}$	1.66	155 ± 9	2.1×10^9	18.8
Regime 2 (O^*-*)	$k_{eff2}((CH_4)^2)/(O_2)$	$CH_4 + O^* + * \xrightarrow{k_{1[O^*-*]}} CH_3^* + OH^*$	$(2k_{1[O^*-*]})/(k_{2bf}K_{2a})$	4.2 ± 0.3^d	79	$1.2 \times 10^{6e}, 5.8 \times 10^{4f}$	106.0 ^g
Regime 3 ($*-*$)	$k_{eff3}(O_2)$	$O_2 + 2^* \xrightarrow{K_{2a}k_{2bf}} 2O^*$	$0.5k_{2bf}K_{2a}$	1.0 ± 0.15^h	$<3 \pm 16$	2800	125.5 ^j
Regime 4 ($*-*$)	$k_{eff4}(CH_4)$	$CH_4 + * + * \xrightarrow{k_{1[*-*]}} CH_3^* + H^*$	$k_{1[*-*]}$	1.69 ^k 1.77 ^l	75 ^k 83 ^l	2.0×10^{4k} 5.9×10^{4l}	114.9 ^k 105.9 ^l

^a Most abundant surface intermediates. ^b Rate and equilibrium constants are defined in Scheme 2. ^c $r_{CH_4}(r_{CD_4})^{-1}$. ^d Effective rate constants ($k_{eff2,H}$, $k_{eff2,D}$) in $r_{CH_4}(r_{CD_4})^{-1}$ term were determined by least-squares regression of $r_{CH_4}(CH_4)^{-1}$ versus CH_4/O_2 (or $r_{CD_4}(CD_4)^{-1}$ versus CD_4/O_2) data. ^e Apparent pre-exponential factor. ^f Pre-exponential factor for C–H bond dissociation, calculated from the apparent pre-exponential factor by assuming identical pre-exponential factors for O_2 activation in regimes 2 and 3. ^g Entropy loss for $CH_4(g)$ upon the formation of $(H_3C^*--*OH)^\ddagger$ transition state structures, calculated by assuming identical pre-exponential factors for O_2 activation in regimes 2 and 3. ^h Effective rate constants in $r_{CH_4}(r_{CD_4})^{-1}$ term determined by least-squares regression of r_{CH_4} versus O_2 pressure (or r_{CD_4} versus O_2 pressure). ⁱ Estimated based on non-activated O_2 dissociation steps (± 195 kPa⁻¹ s⁻¹). ^j Entropy loss for O_2 dissociation steps. ^k CH_4-H_2O (ref 7). ^l CH_4-CO_2 (ref 7).

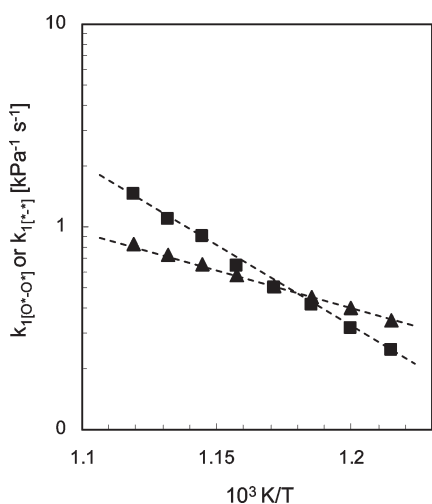


Figure 4. Arrhenius plots of first-order rate constants for CH₄ combustion (■, $k_{1[O^*-O^*]}$; 8.5 nm Pt clusters, 0.15 mg 0.2% wt Pt/Al₂O₃, 2.08 cm³ (STP) s⁻¹)^a and steam reforming (▲, $k_{1[*-*]}$; 1.6% wt Pt/ZrO₂, calculated from kinetic parameters reported in ref 7) on supported Pt clusters.

saturated with O*. At O* saturation, kinetically relevant C–H activation steps are assisted by O* atoms, the number of which is independent of O₂ pressure, to form CH₃O* and OH* (Step 1.1, Scheme 2). CH₄–CD₄ cross exchange rates measured in CH₄–CD₄–O₂ mixtures on 0.2% wt Pt/SiO₂ at 920 K⁵⁵ gave CH₃O* and *OD (or CD₃O* and *OH) recombination rates (reverse of Step 1.1) ~50 times smaller than CH₄ chemical conversion rates, consistent with irreversible C–H bond activation steps. The coverages of species derived from H₂O and CO₂ (OH* and CO*) are small, as evident from the lack of kinetic effects of H₂O and CO₂ pressures (0–5 kPa H₂O or CO₂; Figures 1 and 2).

These data and mechanistic inferences indicate that rates in regime 1 (r_1) are accurately described by a rate equation (derived in Supporting Information)

$$r_1 = k_{1[O^*-O^*]}(CH_4)^1(O_2)^0 \quad (3)$$

in which $k_{1[O^*-O^*]}$ represents the rate constant for C–H bond dissociation elementary steps on O*–O* site pairs (Step 1.1). Equation 3 remains the same whether O₂ dissociation steps (Steps 2.1 and 2.2) are irreversible or quasi-equilibrated because Pt surfaces are saturated with O* (derived in Supporting Information). Oxygen vacancies (*) can participate in C–H bond dissociation, but they are minority species and do not contribute to measured CH₄–O₂ reaction rates in this regime; the kinetically relevant involvement of vacancies would instead cause the rates to increase with decreasing O₂ pressure, in contradiction with the lack of O₂ pressure effects in regime 1.

O* coverages during CH₄–O₂ reactions can be measured by comparing ¹⁸O₂–¹⁶O₂ isotopic exchange rates in the presence and absence of CH₄ reactants. Without CH₄, chemisorbed O* atoms are in equilibrium with O₂(g); thus, their coverages depend only on O₂ pressure. The O*-to-* ratio at chemical equilibrium, $[(O^*)/(*)]_{eq}$, is given by the Langmuir adsorption equation

$$\left(\frac{(O^*)}{(*)}\right)_{eq} = \sqrt{K_{2a}K_{2b}(O_2)} \quad (4)$$

in which K_{2a} and K_{2b} are the equilibrium constants for the O₂ molecular adsorption (k_{2af}/k_{2ar} ; Step 2.1) and O₂* dissociation (k_{2bf}/k_{2br} ; Step 2.2), respectively. O* coverages during steady-state CH₄–O₂ reactions may become lower than equilibrium, because O* can be removed via reactions with CH₄ faster than O* recombination (reverse of Step 2.2). Irreversible C–H bond dissociation on O*–O* pairs (Step 1.1) and reversible O₂ dissociation (Steps 2.1 and 2.2) in regime 1 lead to steady-state O*-to-* ratios, $[(O^*)/(*)]_{ss,1}$, given by

$$\begin{aligned} \left(\frac{(O^*)}{(*)}\right)_{ss,1} &= \sqrt{\frac{K_{2a}k_{2bf}(O_2)}{2k_{1[O^*-O^*]}(CH_4) + k_{2br}}} \\ &= \sqrt{K_{2a}K_{2b}(O_2)_v} \end{aligned} \quad (5)$$

in which the subscript “ss,1” denotes steady-state and regime 1. This equation defines (O₂)_v as a virtual O₂ pressure^{56,57} that reflects, by analogy with eq 4, the “fictitious” O₂ pressure that would give the prevalent O* coverage ($(O^*)_{ss}$) if O₂ adsorption–desorption steps were equilibrated. This virtual pressure acts as a rigorous surrogate for the oxygen chemical potential at catalytic surfaces during chemical conversions.⁵⁸ The concept of virtual pressure and its role in surface reactions^{56,57} have been demonstrated for many catalytic reactions; NH₃ decomposition⁵⁹ and alkane dehydrogenation⁶⁰ catalysis are specific examples. The values of (O₂)_v and $[(O^*)/(*)]_{ss}$ ratios (eq 5) depend on the rate constants for O₂* dissociation (k_{2bf}), O* recombination (k_{2br}), and C–H bond dissociation ($k_{1[O^*-O^*]}$), on the equilibrium constant for molecular O₂ adsorption (K_{2a}), and on the prevalent O₂ and CH₄ pressures. Equations 4 and 5 become identical when $k_{2br} \gg 2k_{1[O^*-O^*]}(CH_4)$, an inequality stating that O* recombination rates (reverse of Step 2.2) are much larger than for C–H bond activation (Step 1.1). In such instances, O₂ adsorption–desorption steps are quasi-equilibrated during CH₄–O₂ reactions; thus, (O₂)_v and O₂ pressures are identical and the oxygen chemical potential at Pt surfaces equals that in the contacting gas phase. When O₂ dissociation steps are irreversible ($k_{2br} \ll 2k_{1[O^*-O^*]}(CH_4)$), O* is predominantly removed via reactions with CH₄ instead of recombination; (O₂)_v values (eq 5) become smaller than the O₂ pressures and $[(O^*)/(*)]_{ss}$ ratios become smaller than at conditions of adsorption–desorption equilibrium (eq 4).

Isotopic ¹⁸O₂–¹⁶O₂ exchange rate ratios with CH₄–¹⁸O₂–¹⁶O₂ and ¹⁸O₂–¹⁶O₂ mixtures reflect the reversibility of O₂ dissociation steps and the (O₂)_v values during catalysis. Steady-state ¹⁶O₂–¹⁸O₂ isotopic exchange rates (at 0.15–1.85 kPa O₂; 873 K) were measured in ¹⁸O₂–¹⁶O₂ and CH₄–¹⁸O₂–¹⁶O₂ mixtures on 0.2% wt Pt/Al₂O₃ samples with 1.8 or 8.5 nm Pt clusters. Pt cluster surfaces are saturated with O* during catalysis at these O₂ pressures (regime 1), as must also be the case in ¹⁸O₂–¹⁶O₂ mixtures at chemical equilibrium in the same O₂ pressure range. ¹⁶O₂–¹⁸O₂ exchange rates at chemical equilibrium ($r_{ex,eq}$) are proportional to (O₂)^{0.5} (Figure 5) on both Pt catalysts, a kinetic dependence consistent with ¹⁸O₂–¹⁶O₂ exchange routes that form ^xO^yO* (x and y are used herein to differentiate 16 and 18 labeled O) via concerted reactions between adsorbed ^xO₂* ($x = 16$ or 18) and vicinal ^yO* ($y = 18$ or 16) (Step 11, Scheme 2). This mechanistic proposal also accounts for the molecular ^xO₂ adsorption (as ^xO₂*) followed by migration of one of the ^xO atoms on Pt surfaces nearly saturated with ^yO*, which may desorb as ^xO^yO before dissociation (to be discussed in section 3.3). It also accounts

for the preferential formation of $^{16}\text{O}^{18}\text{O}(\text{g})$ isotopologues upon exposure of $^{16}\text{O}^*$ covered Pt clusters to $^{18}\text{O}_2(\text{g})$.⁶¹ In contrast, recombinative desorption of two O^* atoms is expected to form predominantly $^{16}\text{O}_2(\text{g})$. The rate of $^{16}\text{O}^{18}\text{O}$ formation from equimolar $^{16}\text{O}_2$ – $^{18}\text{O}_2$ reactant mixtures (derived in Supporting Information) is given by

$$r_{\text{ex,eq}} = \frac{2k_{11f}K_{2a}^{1.5}K_{2b}^{0.5}(\text{O}_2)^{1.5}}{\left(1 + 2\sqrt{K_{2a}K_{2b}}(\text{O}_2) + 2K_{2a}(\text{O}_2)\right)^2} \quad (6a)$$

$\begin{matrix} \uparrow & \uparrow & \uparrow \\ * & \text{O}^* & \text{O}_2^* \end{matrix}$

Each denominator term represents the coverage of the denoted intermediate relative to unoccupied surface atoms. This equation gives the $(\text{O}_2)^{0.5}$ effects on exchange rates ($r_{\text{ex,eq},\text{O}^*}$) when O^* is the MASI, as shown in Figure 5.

$$r_{\text{ex,eq},\text{O}^*} = \frac{k_{11f}}{2} \left(\frac{K_{2a}}{K_{2b}}\right)^{0.5} (\text{O}_2)^{0.5} \quad (6b)$$

No other combination of elementary steps was found to describe the measured O_2 effects on exchange rates for O^* -saturated clusters and the initial formation of $^{16}\text{O}^{18}\text{O}$ species from $^{18}\text{O}_2(\text{g})$ – $^{16}\text{O}^*$ reactions.

$^{16}\text{O}_2$ – $^{18}\text{O}_2$ exchange rates are proportional to $^x\text{O}^*$ ($x = 16$ or 18) and $^y\text{O}_2^*$ ($y = 18$ or 16) coverages, where $^y\text{O}_2^*$ species are in equilibrium with $\text{O}_2(\text{g})$ (Step 2.1). The ratio of isotopic exchange rates for CH_4 – $^{18}\text{O}_2$ – $^{16}\text{O}_2$ ($r_{\text{ex,ss}}$) and $^{18}\text{O}_2$ – $^{16}\text{O}_2$ ($r_{\text{ex,eq}}$) mixtures (denoted as χ) can then be expressed in terms of O^* and $^x\text{O}_2^*$; it reflects the coverages of O^* during steady-state catalysis (O^*)_{ss} relative to those at chemical equilibrium (O^*)_{eq}

$$\chi = \left(\frac{r_{\text{ex,ss}}}{r_{\text{ex,eq}}}\right) = \frac{k_{11f}[(^y\text{O}_2^*)(^x\text{O}^*)]_{\text{ss}}}{k_{11f}[(^y\text{O}_2^*)(^x\text{O}^*)]_{\text{eq}}} \quad (7)$$

$$= \frac{\text{O}_2[(\text{O}^*)(^*)]_{\text{ss}}}{\text{O}_2[(\text{O}^*)(^*)]_{\text{eq}}} = \frac{(\text{O}^*)_{\text{ss}}[1 - (\text{O}^*)_{\text{ss}}]}{(\text{O}^*)_{\text{eq}}[1 - (\text{O}^*)_{\text{eq}}]}$$

where O^* denotes the combined surface coverages of both oxygen isotopes ($^{16}\text{O}^*$ and $^{18}\text{O}^*$). Isotopic exchange rates during CH_4 – O_2 reactions ($r_{\text{ex,ss}}$) are also given by eq 6b, except that $(\text{O}_2)_v$ replaces the (O_2) terms. Taken together with eq 5, eq 7 (for χ in regime 1; χ_1) can be written in terms of CH_4 pressure and the relevant kinetic ($k_{1[\text{O}^*-\text{O}^*]}$, $k_{2\text{br}}$, $k_{2\text{bf}}$) and thermodynamic (K_{2b}) constants defined in Scheme 2

$$\chi_1 = \left(\frac{r_{\text{ex,ss,1}}}{r_{\text{ex,eq}}}\right) = \frac{(\text{O}^*)_{\text{ss,1}}[1 - (\text{O}^*)_{\text{ss,1}}]}{(\text{O}^*)_{\text{eq}}[1 - (\text{O}^*)_{\text{eq}}]} \quad (8)$$

$$= \sqrt{\frac{(\text{O}_2)_v}{(\text{O}_2)}} = \sqrt{\frac{k_{2\text{bf}}}{[2k_{1[\text{O}^*-\text{O}^*]}(\text{CH}_4) + k_{2\text{br}}]K_{2b}}}$$

$^{16}\text{O}^{18}\text{O}$ formation rates were measured during CH_4 – $^{16}\text{O}_2$ – $^{18}\text{O}_2$ reactions in regime 1 (O_2/CH_4 ratios larger than 0.3 and 2 for 1.8 and 8.5 nm Pt clusters, respectively) at 873 K. These rates, shown as their corresponding rate constants ($0.5k_{11f}(K_{2a}/K_{2b})^{0.5}$; eq 6b) in Figure 5, are similar to those measured at chemical equilibrium with CH_4 -free $^{18}\text{O}_2$ – $^{16}\text{O}_2$ reactants. Thus, χ_1 (eq 8) is

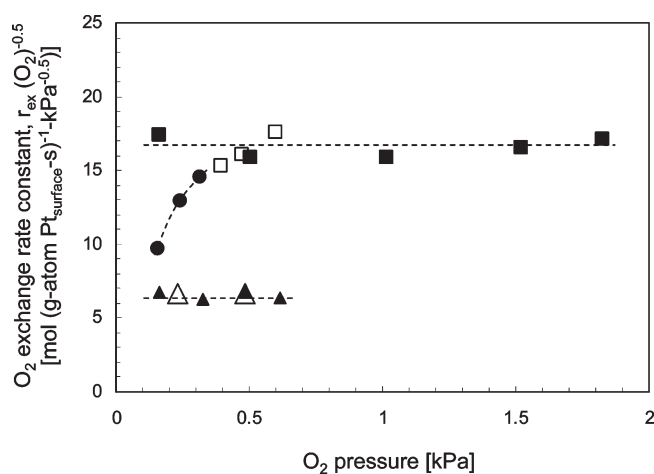


Figure 5. Isotopic oxygen-exchange rate constants ($r_{\text{ex}}(\text{O}_2)^{-0.5}$) of 0.2% wt Pt/ Al_2O_3 (1.8 nm (\blacktriangle , \triangle) and 8.5 nm (\blacksquare , \square , \bullet) Pt clusters) during $^{16}\text{O}_2$ – $^{18}\text{O}_2$ (\blacktriangle , \blacksquare) and CH_4 – $^{16}\text{O}_2$ – $^{18}\text{O}_2$ (\triangle , \square , \bullet) reactions in kinetic regimes 1 (\triangle , \square) and 2 (\bullet) at 873 K. (200 SiO₂/catalyst intraparticle (λ) and 4700 quartz/catalyst interparticle (χ) dilution ratios, 2.08 cm³ (STP) s⁻¹, 0.25–1.6 kPa CH₄ for CH_4 – $^{16}\text{O}_2$ – $^{18}\text{O}_2$ (\triangle , \square) reactions, $^{16}\text{O}_2/^{18}\text{O}_2 = 1$. Regime 1: O_2/CH_4 ratios of >0.3 and >2 for 1.8 and 8.5 nm Pt clusters, respectively; regime 2: $\text{O}_2/\text{CH}_4 < 2$ for 8.5 nm Pt clusters).

essentially unity throughout regime 1 and $(\text{O}_2)_v$ and O_2 pressures are therefore identical. These results confirm that O_2 dissociation steps are quasi-equilibrated during CH_4 – O_2 reaction ($2k_{1[\text{O}^*-\text{O}^*]}(\text{CH}_4) \ll k_{2\text{br}}$ in eqs 5 and 8) and that CH_4 reactions with O^* in regime 1 are too slow to perturb the equilibrium O^* coverages.

$(\text{O}_2)_v$ (also the prevalent O_2 pressure in regime 1) acts as a rigorous surrogate for the oxygen chemical potential at Pt cluster surfaces and determines the O^* coverages and relative abundances of O^*-O^* , $\text{O}^*-\text{*}$, and $\text{*}-\text{*}$ sites; it also reflects the thermodynamic tendency of such clusters to undergo bulk oxidation during CH_4 – O_2 catalysis. Thermodynamic data for Pt, Pt₃O₄, and PtO₂ bulk structures⁶² give the O_2 pressures required for Pt–Pt₃O₄ and Pt₃O₄–PtO₂ phase transitions. Assuming thermodynamic properties of the larger Pt clusters (8.5 nm) used here resemble those of large Pt crystallites, extrapolation of the Pt–Pt₃O₄ phase diagram⁶² to 873 K indicates that these Pt clusters retain a metallic bulk at O_2 pressures below ~800 kPa, including those used in this study (<23 kPa). The size of the Pt cluster may affect its thermodynamic tendency to form bulk oxides. Small clusters (<3 nm) contain a larger fraction of coordinatively unsaturated corner and edge sites that bind O^* more strongly than the more coordinatively saturated terrace sites prevalent on large clusters. The stronger binding of O^* and larger O^* -to-overall Pt atomic ratios inherent in these small clusters may cause them to exhibit oxide-like properties well below the $(\text{O}_2)_v$ required for bulk Pt oxidation. The bulk oxidation is expected to cause marked changes in rates in response to a transition in active site structures and kinetically relevant step. Such changes have been established on Pd;⁶³ they lead to exposed Pd²⁺ atoms on PdO surfaces that interact strongly with CH₃ groups at the transition state and, in turn, lower the C–H bond activation barriers.^{64–66} These catalytic consequences of phase transition were, however, not detected on Pt clusters (1.8–8.5 nm) under the conditions of our study ($0 < \text{O}_2/\text{CH}_4 < 10$; 873 K) and, consistent

Table 2. Average Pt Coordination Numbers, Oxygen Binding Strengths on Uncovered and O* Saturated Pt Clusters (201 atoms, 1.8 nm diameter), C–H Bond Activation Barriers on O*–O* Site Pairs (regime 1), and the Energies Required to Promote O* to Reactive Bridge Sites ($\Delta E_{\text{O}^* \text{ promotion}}$) for the Various Types of O* Atoms on Pt₂₀₁ Clusters

O* ^a	average coordination number of Pt atoms interact with the O*	O* binding strength on uncovered clusters (kJ mol ⁻¹)	O* binding strength at O* saturation ^b (kJ mol ⁻¹)	$\Delta E_{\text{O}^* \text{ promotion}}$ ^c (kJ mol ⁻¹)	C–H bond activation barrier on O*–O* site pair (kJ mol ⁻¹)
I	6.50	410	368	13	112
II	7.33	391	426	67	175
III	7.50	383	353	9	111
IV	8.33	375	352	99	170
V	9.00	372	271	44	149

^a Refer to Scheme 1 for the placement of O* atom. ^b Defined by the O*/O*_{max} atomic ratio equals 1 where O*_{max} is the total number of O* adsorption sites (sites I–V) on the Pt₂₀₁ cluster. ^c Energies required to promote the O* atom from the stable adsorption site to interact with the H.

with Pt clusters remain in metallic state under stronger oxidation tendencies at much higher O₂ pressures (101 kPa) and lower temperatures (698 K).⁶¹ The guidance from O₂–Pt thermodynamics, taken together with the zero-order O₂ dependence of rates and the excellent agreement between experimental activation barriers to those calculated on metallic Pt cluster surfaces saturated with O* (to be shown next), indicate that Pt clusters remain metallic and that the structure and phase of these clusters do not change within the range of O₂ pressures that define regime 1. The formation of two-dimensional surface oxides⁶⁷ would cause significant catalytic consequences, which are not detected on Pt, but which we have observed for clusters of less noble metals (Pd,⁶⁴ Rh⁶⁸). Thus, we conclude that these surface oxides, if they form, would do so at oxygen chemical potentials closer to the Pt–PtO transition and well above those of relevant to CH₄–O₂ catalysis.

These rate data and their mechanistic interpretations, together with thermodynamic guidance, indicate that CH₄ reaction rates in regime 1 are limited by C–H bond activation on O*-saturated surfaces, in a step that uses O*–O* site pairs to form CH₃O* and OH* (Step 1.1, Scheme 2). The barriers and reaction energies for this step can be estimated for different O*–O* site pairs on (111) and (100) facets of 1.8 nm Pt₂₀₁ clusters saturated with O* atoms (refers to Scheme 1 for the placements of O* atoms at sites I–V and the structure of the Pt₂₀₁ cluster) using density functional theory. Chemisorbed O* atoms preferentially reside at five distinct adsorption sites on Pt₂₀₁ clusters:²⁶ threefold fcc sites (types II, IV, and V) on (111) facets and bridge sites (types I and III) on (100) facets, as also found to be the most stable O* adsorption sites on single crystal Pt(111) and Pt(100) surfaces,^{69–71} respectively. O* binding energies at sites I–V on bare Pt₂₀₁ clusters range from 372 kJ mol⁻¹ to 410 kJ mol⁻¹ (Table 2), depending on the location of the O* atoms (fcc or bridge) and the coordination of the Pt atoms to which the O* atom is bound.²⁶

At O* saturation, binding energies for O* at each position are much smaller than on bare clusters because of lateral repulsion between coadsorbed oxygen as summarized in Table 2. One exception occurs at site II where Pt–Pt distances at these coordinatively unsaturated corner sites expand from 0.270 to 0.315 nm with increasing O* coverages. The neighboring oxygen atoms that bind to the same Pt site are located on the adjacent facets; such configurations remove through space repulsive interactions between the O* atoms. These combined effects lead to stronger Pt–O interactions at O* saturation (426 kJ mol⁻¹ vs 391 kJ mol⁻¹ for O* saturated and uncovered Pt₂₀₁ clusters, respectively). The saturation oxygen coverage for Pt₂₀₁ clusters (O*/O*_{max} = 1) corresponds to an O*/Pt_s (where Pt_s denotes surface Pt atom)

ratio of 1.08, a value much larger than at O* saturation on Pt(111) single crystals (0.5–0.73 O* ML^{67,72} depending on the oxygen source). In contrast, higher O* coverages on Pt(111) lead to unfavorable adsorption of oxygen, indicated by the differential O* adsorption energies (defined by $Q_{\text{O}^*} = -\Delta H_{\text{O}^*}$ for $\text{O} + n \text{O}^*/\text{Pt}_{201} \rightarrow (n+1) \text{O}^*/\text{Pt}_{201}$ reaction) larger than zero on 0.89 O* ML Pt(111) surfaces in contrast to less than zero (–37 kJ mol⁻¹) on the Pt₂₀₁ clusters. The lower O* saturation coverages on the (111) surface reflect, at least in part, the lateral rigidity of extended surfaces, which preserves aligned structures that maximize lateral repulsion and prevent the attainments of higher coverages. In contrast, Pt clusters form surface structures with O*/Pt_s ratios near unity, as found experimentally even at low O₂ pressures,⁷³ because the small dimensions of exposed low-index planes allow lateral flexibility in O* monolayers and relieve repulsive interactions to some extent, while also providing more coordinatively unsaturated surface atoms that form stronger O*–Pt bonds. Cubooctahedral clusters were found here to expand radially as O* coverages increased, thus increasing the distance between oxygen atoms further and minimizing their interactions.

Next, we probe the details of C–H bond activation steps on O*–O* site pairs and the roles of O* binding strength on their reactivity for H-abstraction (Step 1.1) on Pt₂₀₁ clusters saturated with O* (O*/O*_{max} = 1). Irrespective of the location and binding energy of O*, these species activate C–H bonds via hydrogen abstraction paths similar to that shown in Figure 6 for O* atoms at threefold terrace sites (site V, Scheme 1) in the (111) facet. This step has a reaction energy of –54 kJ (mol CH₄)⁻¹ and proceeds via H-abstraction from CH₄ by one of the O* atoms in the O*–O* site pair, in a step mediated by a late transition state in which the C–H bond is nearly cleaved (0.170 nm vs 0.109 nm in CH₄(g)) and the O–H bond is almost formed (0.105 nm vs 0.099 nm in OH* product). The O* atom involved in H-abstraction moves from its stable threefold fcc site to a less stable and more reactive bridge site along the reaction coordinate in a step that is significantly endothermic ($\Delta E_{\text{O}^* \text{ promotion}} = 44 \text{ kJ mol}^{-1}$). The CH₃ formed in the H-abstraction step exhibits sp² hybridization and free radical character and coordinates weakly to the H-atom in the O–H species that concurrently forms at the transition state. The large distance between the CH₃• fragment and the other O* in the O*–O* site pair (0.265 nm) indicates that CH₃• interacts very weakly with both the O* and OH* species and is essentially unbound at the transition state.

C–H activation barriers on different O*–O* site pairs on Pt₂₀₁ clusters range from 111 to 175 kJ mol⁻¹ (Table 2) and depend on the average coordination number of the metal atoms

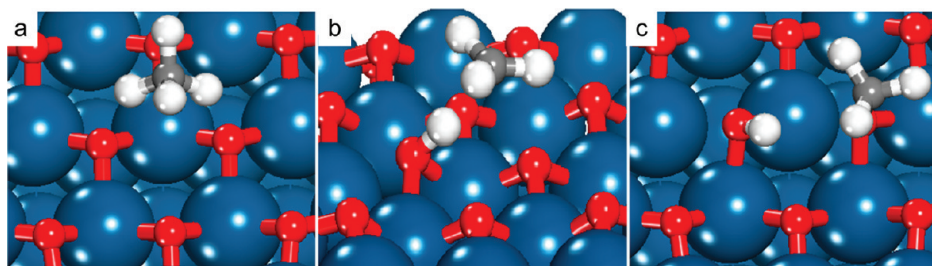


Figure 6. Structures of reactant (a, $\text{CH}_4(\text{g})$, O^*-O^*), transition state (b, $\text{O}^*-\text{CH}_3^*-\text{OH}^*$), and product (c, CH_3O^* , OH^*) for the initial C–H bond dissociation of CH_4 on O^*-O^* site pairs formed from two O^* atoms chemisorbed at terrace sites (sites V, Scheme 1) of the (111) facet of a Pt_{201} cluster saturated with chemisorbed oxygen atoms ($\text{O}^*/\text{O}_{\text{max}} = 1$). O–H, C–H, and O–C bond lengths of the $\text{O}^*-\text{CH}_3^*-\text{OH}^*$ transition state complex are 0.104 nm, 0.170 nm, and 0.265 nm, respectively. (See Supporting Information Figure S-1 for the view of the entire Pt cluster).

to which the O^* atoms are bound, the number of O^* neighbors, as well as the specific locations of the O^* neighbors that surround this site. These sites can be grouped into three types: (a) bridging O^* sites (I and III) with barriers of 111–112 kJ mol^{-1} , (b) corner and edge O^* sites (II and IV) with barriers of 170–175 kJ mol^{-1} , and (c) terrace sites (V) with barriers of 149 kJ mol^{-1} . The structural details of the reactant, transition, and product states for each of these site pairs are shown in Supporting Information (Table S-1). O^* atoms at bridge sites on 100 facets (I and III) gave the lowest C–H bond activation barriers because they lie closest to the active bridge-bound O^* present at all H-abstraction transition states; as a result, they require the smallest energies for promotion to their active locations ($\Delta E_{\text{O}^* \text{ promotion}} = 9\text{--}13 \text{ kJ mol}^{-1}$). O^* atoms at corner and edge sites on (111) facets (sites II and IV, respectively) are the least reactive because their binding to low-coordination Pt atoms at threefold sites makes their promotion to active location very endothermic (67–99 kJ mol^{-1}). O^* atoms at (111) terrace sites (V) are more weakly held than those at corner and bridge sites (II and IV) because of the higher Pt coordination (average Pt coordination number $\langle \text{CN} \rangle = 9$) than at threefold edge ($\langle \text{CN} \rangle = 8.33$) and corner ($\langle \text{CN} \rangle = 7.50$) sites. These O^* atoms (V) are also less strongly bound than at sites on (100) facets ($\langle \text{CN} \rangle$ of 6.5 for site I and 7.50 for site III). The more weakly held O^* at (111) terrace sites (V) are more basic and show greater proton affinity, but the energy required to promote them to the active bridge location ($\Delta E_{\text{O}^* \text{ promotion}} = 44 \text{ kJ mol}^{-1}$) is 31–35 kJ mol^{-1} larger than for O^* at bridge sites on (100) facets, but 23–55 kJ mol^{-1} smaller than at corner and edge sites. As a result, C–H activation barriers on these O^* atoms (V; 149 kJ mol^{-1}) lie between the barriers on edge and corner sites (170–175 kJ mol^{-1}) and on (100) facets (111–112 kJ mol^{-1}). These C–H activation barriers can be rigorously interpreted using Born–Haber thermochemical cycles that account for the properties of O^* and Pt atoms and also for the local O^* interactions, as will be discussed in detail in later studies.

O^* at (111) facets of Pt_{201} clusters (site V) are the most abundant species on O^* -saturated surfaces of Pt clusters with diameters larger than 5 nm (>70% assuming cuboctahedral geometries⁵⁰). Indeed, C–H activation barriers at such sites (149 kJ mol^{-1}) are very similar to the barriers measured on 8.5 nm Pt clusters (155 kJ mol^{-1} ; Table 1). Low coordination Pt atoms associated with the corner and edge sites (sites II and IV) become more abundant with decreasing cluster size (70% of exposed atoms in a 1.5 nm cuboctahedral cluster reside at corner and edge sites⁵⁰); activation barriers will increase and rates decrease with decreasing cluster size, the

latter trend of which was observed experimentally (to be discussed in section 3.6).

C–H bond activation barriers on O^*-O^* site pairs (theory: 149 kJ mol^{-1} for O^* atoms at the terrace sites (type V), experiment: 155 kJ mol^{-1}) are much larger than on $^*-\text{O}^*$ site pairs (theory: 79 kJ mol^{-1} ,²⁶ experiment: 75 kJ mol^{-1} ($\text{CH}_4-\text{H}_2\text{O}$) and 83 kJ mol^{-1} (CH_4-CO_2)⁷). The large differences, however, do not cause commensurate differences in measured C–H bond activation rate constants, which were 1.1 $\text{kPa}^{-1} \text{ s}^{-1}$ ($k_{1[\text{O}^*-\text{O}^*]}$, in CH_4-O_2 mixtures, regime 1) and 0.6 $\text{kPa}^{-1} \text{ s}^{-1}$ ($k_{1[^*-\text{O}^*]}$, in $\text{CH}_4-\text{H}_2\text{O}$ mixtures, regime 4)⁷ at 873 K. The large barriers on O^*-O^* site pairs are compensated by large pre-exponential factors: measured pre-exponential factors are much larger in regime 1 ($2.1 \times 10^9 \text{ kPa}^{-1} \text{ s}^{-1}$) than on the $^*-\text{O}^*$ site pairs prevalent in regime 4 (Step 1.3, $2.0 \times 10^4 \text{ kPa}^{-1} \text{ s}^{-1}$ ($\text{CH}_4-\text{H}_2\text{O}$) and $5.9 \times 10^4 \text{ kPa}^{-1} \text{ s}^{-1}$ (CH_4-CO_2), Table 1) and also larger than estimates from the transition state theory⁷⁴ by assuming the loss of one translational mode at the transition state ($2.2 \times 10^4 \text{ kPa}^{-1} \text{ s}^{-1}$). The large pre-exponential factors reflect small negative activation entropies ($\Delta S = -18.8 \text{ J mol}^{-1} \text{ K}^{-1}$, experimental, Table 1) resulted from the weakly bound CH_3 at the transition state retaining most of the $\text{CH}_4(\text{g})$ translational entropy. This entropy–enthalpy compensation accounts for the similar rate constant values measured for CH_4-O_2 and $\text{CH}_4-\text{H}_2\text{O}$ reactions in the temperature range of catalytic relevance (Figure 4). The small entropic losses, high barriers (130–150 kJ mol^{-1}), and radical-like transition states are general for C–H bond activation at O^*-O^* sites on Pd metal clusters²⁷ and on $\alpha\text{-PtO}_2$ (0001), RhO_2 (110), and Rh_2O_3 (001) surfaces when oxygen vacancies (*) are unavailable to stabilize CH_3 groups at oxygen sites.⁷⁵ Such radical-like transition states are also found for C–H bond activation in larger alkanes on oxide structures⁷⁶ and detected during oxidative coupling of CH_4 on nonreducible Li–MgO catalysts, in which methyl radicals actually desorb onto the gas phase and react via homogeneous coupling and oxidation reactions.⁷⁷

3.3. Kinetically Relevant C–H Bond Activation on Pt Surfaces at Intermediate O^* Coverages (Kinetic Regime 2). We consider next the catalytic consequences of oxygen vacancies (*), which form within O^* monolayers as the O_2/CH_4 reactant ratio decreases and the reverse rates of the O_2 dissociation steps become lower than the CH_4 activation rates. Specifically, we address the kinetic and mechanistic evidence for the involvement of vacancy sites (*), which can stabilize the CH_3 fragment in C–H bond activation transition states and lead to >100-fold increases in rates as O_2/CH_4 ratios decrease from 9.5 to 0.08 (Figure 3). Vacancies with vicinal O^* species form O^*-O^* site

pairs that combine the role of O* in H-abstraction and the binding of CH₃ in a manner that stabilizes the energies of the (*-CH₃-H-O*)[‡] transition states. Such concerted O*-H and *-CH₃ interactions lead to more effective C-H bond activation on O*-* than on O*-O* site pairs (Steps 1.2 and 1.1, respectively, Scheme 2), as also proposed for the kinetically relevant C-H bond activation step in CH₄-O₂ reactions on PdO_x⁷⁸ and C₂H₆-O₂⁷⁹ and CH₃OCH₃-O₂ reactions on Pt.⁴⁴

The effects of CH₄ and O₂ pressures on rates in regime 2 (Figures 1 and 2) are consistent with the rate equation derived from pseudo steady-state treatments of all intermediates and the assumptions of irreversible steps for C-H bond dissociation on O*-* site pairs, quasi-equilibrated molecular O₂ adsorption and O* migration, and irreversible O₂* dissociation (Scheme 2)

$$r_{O^*-*} = \frac{0.5k_{2bf}K_{2a}(O_2)}{\left(1 + \frac{k_{2bf}K_{2a}(O_2)}{2k_{1[O^*-*]}(CH_4)}\right)^2} \quad (9)$$

This rate equation contains the rate constants for O₂ and CH₄ dissociation ($k_{1[O^*-*]}$, k_{2bf}) and the equilibrium constant for nondissociative O₂ adsorption (K_{2a}). K_{11} is omitted in this equation because it equals unity and does not modify the form of the rate equation (to be discussed later in this section). In contrast, assumptions of irreversible C-H bond dissociation and quasi-equilibrated O₂ dissociation steps (as in regime 1) lead to rates proportional to CH₄ pressure (derivation in Supporting Information)

$$r_{O^*-*} = \frac{k_{1[O^*-*]}(CH_4)[K_{2a}K_{2b}(O_2)]^{0.5}}{[1 + (K_{2a}K_{2b}(O_2))^{0.5}]^2} \quad (10)$$

in contradiction with rates that depend more sensitively on CH₄ pressure (Figure 1b). The strong dependence on CH₄ pressures suggests that the second denominator term in eq 9 is much larger than 1 and that cluster surfaces are nearly saturated with O* ((O*)/(*) ≫ 1), in which case rates are given by

$$r_2 = k_{1[O^*-*]}(CH_4) \left[\frac{2k_{1[O^*-*]}(CH_4)}{(k_{2bf}K_{2a})(O_2)} \right] \quad (11)$$

The second parentheses term in this equation represents the fraction of Pt atoms that are uncovered (*), which is set by the kinetic coupling of irreversible CH₄ and O₂ activation steps. The emergence of vacancy sites with decreasing O₂/CH₄ ratio leads to the preferential activation of C-H bonds by O*-* site pairs, on which transition states benefit from the O* role in H-abstraction and the * role in CH₃ stabilization. The strong CH₄ pressure effects on rates in this regime 2 (eq 11) arise from the dual role of CH₄ in determining collision rates with surfaces and the likelihood that surfaces contain vacancy sites.

The irreversible nature of C-H bond dissociation steps on O*-* site pairs was confirmed from the absence of CH₄-CD₄ isotopic scrambling in CH₄-CD₄-O₂ mixtures at all O₂/CH₄ ratios and conversions in regime 2. The ratios of CH_{4-x}D_x isotopologue formation rates, which reflect the rates of CH_{3-y}D_y*-OD* and CD_{3-z}H_z*-OH* recombination (reverse of Step 1.2) to those of CH₄ chemical conversion rates, were much less than 1 (~0.01 at 918 K), consistent with net C-H

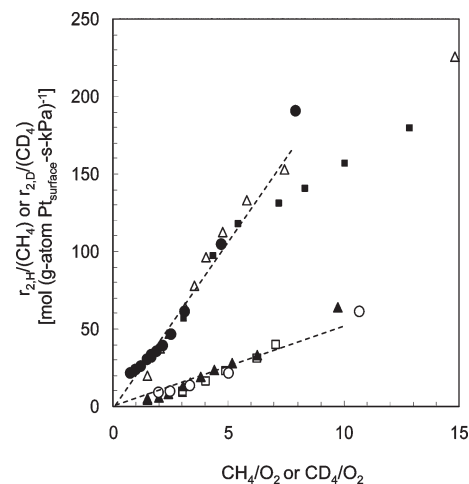


Figure 7. Pseudo first-order rate constants ($r_{2,H}(CH_4)^{-1}$ or $r_{2,D}(CH_4)^{-1}$) during CH₄ (or CD₄) reactions with O₂ on Pt clusters (8.5 nm average cluster size) in kinetic regime 2 as a function of CH₄/O₂ (or CD₄/O₂) ratios. (1.2 kPa (●), 2.4 kPa (△), 4.8 kPa (■) CH₄; 0.8 kPa (○), 2.4 kPa (▲), 4.8 kPa (□) CD₄). (0.15 mg 0.2% wt Pt/Al₂O₃, 873 K, 200 SiO₂/catalyst intraparticle (λ) and 4700 quartz/catalyst interparticle (χ) dilution ratios, 2.08 cm³ (STP) s⁻¹).

dissociation rates that are much larger than for its reverse reaction. We conclude from these data that C-H bond dissociation steps on O*-* pairs (Step 1.2) prevalent in regime 2 are irreversible, as also found in the case of CH₄ reactions in regimes 1 and 4.

The kinetic and thermodynamic parameters (k_{2bf} , $k_{1[O^*-*]}$, and K_{2a}) in eq 11 remain essentially unchanged over the broad range of O₂/CH₄ ratios that defines regime 2 (0.17 < O₂/CH₄ < 2 for 8.5 nm Pt clusters) because (*) sites remain isolated and similar in reactive properties at the near saturation O* coverages prevalent throughout this regime. Cluster surfaces behave as uniform structures in this dilute vacancy regime and can be rigorously treated by Langmuir formalisms of adsorption and surface reactions. Measured pseudo first-order rate constants ($r_2(CH_4)^{-1}$) in regime 2 are proportional to CH₄/O₂ ratios (Figure 7), consistent with eq 11, which is derived based on uniform Langmuirian surfaces, irreversible C-H bond activation on O*-* site pairs and O₂* dissociation, and O* as the most abundant surface species. At higher CH₄/O₂ ratios (>6), oxygen vacancies become abundant, causing the assumptions of O* as MASI and of uniform surfaces to become inaccurate and interactions among vicinal vacancies to influence the reactivity of the neighboring oxygen and the ensemble size of the sites available for CH₃ stabilization, as shown by DFT calculations described below.

The kinetic and isotopic studies reported next were carried out at CH₄/O₂ ratios between 0.5 and 6, for which O* coverages are near saturation, vacancies are dilute, and surfaces behave uniformly. The apparent rate constant in regime 2 ($k_{app,2} = 2k_{1[O^*-*]}^2(k_{2bf}K_{2a})^{-1}$; eq 11) estimated from the slope of the rate data in Figure 7 (873 K, 8.5 nm average Pt cluster size), is 22.0 ± 0.5 mol CH₄ [(g-atom Pt)_{surface}]⁻¹ s⁻¹ kPa⁻¹. The ratio of the effective rate constants for reactions of CH₄ ($(k_{app,H})_2$) and CD₄ ($(k_{app,D})_2$) with O₂ in regime 2 is given by the ratio of the slopes of the respective rate data in Figure 7 for these two methane isotopologues. This ratio gives the CH₄/CD₄ kinetic isotope effect in regime 2 (KIE₂) and reflects the effects

of isotopic substitution on the rate and equilibrium constants that determine these effective rate constants

$$\text{KIE}_2 = \left(\frac{k_{\text{app-H}}}{k_{\text{app-D}}} \right)_2 = \left(\frac{k_{1[\text{O}^*-\text{*}]\text{-H}}}{k_{1[\text{O}^*-\text{*}]\text{-D}}} \right)^2 \left(\frac{(k_{2\text{bf}}K_{2\text{a}})_{\text{D}}}{(k_{2\text{bf}}K_{2\text{a}})_{\text{H}}} \right)^4 \quad (12)$$

The large KIE value of 4.2 ± 0.3 at 873 K confirms the kinetic relevance of C–H bond activation in this regime. The O_2 adsorption equilibrium constant ($K_{2\text{a}}$) and the O_2 dissociation rate constant ($k_{2\text{bf}}$) do not depend on the reductant identity (CH_4 or CD_4); thus, $K_{2\text{a-H}}/K_{2\text{a-D}}$ and $k_{2\text{bf-H}}/k_{2\text{bf-D}}$ in eq 12 are unity and the first term in this equation ($k_{1[\text{O}^*-\text{*}]\text{-H}}/k_{1[\text{O}^*-\text{*}]\text{-D}}$) is responsible for the observed H/D effects on reaction rates. The measured isotope effects are significantly larger than for C–H bond activation steps on O^* -saturated surfaces (1.66, regime 1) or on uncovered surfaces (1.69 ($\text{CH}_4\text{-H}_2\text{O}$) and 1.77 ($\text{CH}_4\text{-CO}_2$), regime 4)⁷ because the ratio of rate constants appears as a square term (eq 12) in regime 2, but as a linear term in regimes 1 and 4 ($k_{1[\text{O}^*-\text{*}]\text{-H}}/k_{1[\text{O}^*-\text{*}]\text{-D}}$ and $k_{1[\text{*}-\text{*}]\text{-H}}/k_{1[\text{*}-\text{*}]\text{-D}}$, respectively). The KIE value in regime 2, however, is slightly larger than expected from the square of the KIE values in regimes 1 and 4 ($(k_{1[\text{O}^*-\text{*}]\text{-H}}/k_{1[\text{O}^*-\text{*}]\text{-D}})^2$ or $(k_{1[\text{*}-\text{*}]\text{-H}}/k_{1[\text{*}-\text{*}]\text{-D}})^2$, $\sim 2.9\text{--}3.3$). These stronger isotope effects may reflect a larger difference between the energies for $(\text{H}_3\text{C}^*-\text{*}\text{OH})^\ddagger$ and $(\text{D}_3\text{C}^*-\text{*}\text{OD})^\ddagger$ activated complexes than those for $(\text{H}_3\text{CO}^*-\text{*}\text{OH})^\ddagger$ and $(\text{D}_3\text{CO}^*-\text{*}\text{OD})^\ddagger$ and for $(\text{H}_3\text{C}^*-\text{*}\text{H})^\ddagger$ and $(\text{D}_3\text{C}^*-\text{*}\text{D})^\ddagger$, which are formed during the C–H bond activation steps on O^*-O^* (regime 1) and $\text{*}-\text{*}$ (regime 4) site pairs, respectively. We surmise that the strong KIE effects are caused in part by the formation of an earlier transition-state structure than those occurring on O^*-O^* and $\text{*}-\text{*}$ site pairs, as suggested by the shorter C–H bond length {0.129 nm ($\text{O}^*-\text{*}$ site pairs) vs 0.170 nm (O^*-O^* site pairs) and 0.152 nm ($\text{*}-\text{*}$ site pairs)²⁶} in the $(\text{H}_3\text{C}^*-\text{*}\text{OH})^\ddagger$ transition state, derived from DFT calculations on Pt_{201} clusters.

The apparent activation energy ($E_{\text{app},2}$; regime 2) measured from temperature effects on the effective rate constants, $2k_{1[\text{*}-\text{*}]}^2(k_{2\text{bf}}K_{2\text{a}})^{-1}$ (eq 11), is $89 \pm 20 \text{ kJ mol}^{-1}$. Its value reflects the combined effects of the C–H activation barrier on $\text{O}^*-\text{*}$ site pairs ($E_{1[\text{O}^*-\text{*}]}$), the O_2^* dissociation barrier ($E_{2\text{bf}}$), and the heat of molecular O_2 adsorption (Q_{O_2})

$$E_{\text{app},2} = 2E_{1[\text{O}^*-\text{*}]} - (E_{2\text{bf}} - Q_{\text{O}_2}) \quad (13)$$

The individual contributions cannot be discerned from experiments, but DFT calculations on the various types of sites at Pt_{201} clusters provide significant insights into this matter and into the effects O^* and CH_3^* binding strengths on individual barriers, as well as theoretical support for the mechanistic conclusions based on experiments, as shown later in this section.

Next, we examine the reversibility of O_2 dissociation steps and the O^* coverages prevalent during $\text{CH}_4\text{-O}_2$ reactions in regime 2. We first derive a general expression for the oxygen virtual pressure, $(\text{O}_2)_v$, which relates O^* coverages during catalysis to CH_4 and O_2 pressures in this kinetic regime. A pseudo steady-state balance on reactive O^* intermediates with kinetically relevant C–H bond activation occurring via parallel routes on O^*-O^* , $\text{O}^*-\text{*}$, and $\text{*}-\text{*}$ ⁸⁰ site pairs

(Steps 1.1–1.3) gives

$$2k_{1[\text{O}^*-\text{*}]}(\text{O}^*)(\text{*}) + 2k_{1[\text{O}^*-\text{O}^*]}(\text{O}^*)^2 + 2k_{1[\text{*}-\text{*}]}(\text{*})^2 = k_{2\text{bf}}K_{2\text{a}}\left(\frac{\text{O}_2}{\text{CH}_4}\right)(\text{*})^2 - k_{2\text{br}}\left(\frac{\text{O}^*}{\text{CH}_4}\right)^2 \quad (14)$$

which depends on the CH_4 and O_2 pressures, the equilibrium constant for molecular O_2 adsorption ($K_{2\text{a}}$), and the rate constants for the three C–H bond activation routes ($k_{1[\text{O}^*-\text{O}^*]}$, $k_{1[\text{O}^*-\text{*}]}$, $k_{1[\text{*}-\text{*}]}$) and for O_2^* dissociation ($k_{2\text{bf}}$) and recombination ($k_{2\text{br}}$), as defined in Scheme 2. This quadratic equation can be solved to give a general expression for the $(\text{O}^*)/(\text{*})$ ratio during steady-state catalysis and the defining equation for the virtual O_2 pressure $((\text{O}_2)_v)$, as a rigorous measure of the oxygen chemical potential on catalytic surfaces

$$\begin{aligned} \left[\frac{(\text{O}^*)}{(\text{*})} \right]_{\text{ss}} = & \left[-2k_{1[\text{O}^*-\text{*}]} \pm \left\{ \left[2k_{1[\text{O}^*-\text{*}]}(\text{CH}_4) \right]^2 \right. \right. \\ & - 4 \left[2k_{1[\text{O}^*-\text{O}^*]}(\text{CH}_4) + k_{2\text{br}} \right] \left[2k_{1[\text{*}-\text{*}]}(\text{CH}_4) \right. \\ & \left. \left. - K_{2\text{a}}k_{2\text{bf}}(\text{O}_2) \right] \right\}^{1/2} \left. \right] / \left[2 \left[2k_{1[\text{O}^*-\text{O}^*]}(\text{CH}_4) + k_{2\text{br}} \right] \right] \\ \left(\frac{\text{O}^*}{(\text{*})} \right)_{\text{ss}} = & \sqrt{K_{2\text{a}}K_{2\text{b}}(\text{O}_2)_v} \quad (15) \end{aligned}$$

When the O^* recombination is fast relative to the C–H bond activation

$$k_{2\text{br}}(\text{O}^*)^2 \gg k_{1[\text{O}^*-\text{O}^*]}(\text{CH}_4)(\text{O}^*)^2, \quad k_{1[\text{O}^*-\text{*}]}(\text{CH}_4)(\text{O}^*)(\text{*}), \quad k_{1[\text{*}-\text{*}]}(\text{CH}_4)(\text{*})^2 \quad (16)$$

Equation 15 simplifies to eq 4, in which case $(\text{O}_2)_v$ becomes equal to the prevalent O_2 pressure. This inequality thus defines the conditions required for quasi-equilibrated O_2 dissociation steps when C–H bond activation can occur in parallel by any of the postulated site pairs in the various kinetic regimes. The effects of O_2 and CH_4 pressures on rates suggest that C–H bonds predominantly dissociate on $\text{O}^*-\text{*}$ site pairs in regime 2, at rates much higher (up to 160 times) than on the O^*-O^* (regime 1, Figure 2) and $\text{*}-\text{*}$ site pairs (regime 4, Figure 1)

$$k_{1[\text{O}^*-\text{*}]}(\text{O}^*)(\text{*}) \gg k_{1[\text{O}^*-\text{O}^*]}(\text{O}^*)^2, \quad k_{1[\text{*}-\text{*}]}(\text{*})^2 \quad (17a)$$

This inequality, together with the irreversible O_2 activation steps⁸¹

$$k_{1[\text{O}^*-\text{*}]}(\text{CH}_4)(\text{O}^*)(\text{*}) \gg k_{2\text{br}}(\text{O}^*)^2 \quad (17b)$$

simplifies eq 15 to

$$\left(\frac{\text{O}^*}{(\text{*})} \right)_{\text{ss}} = \sqrt{K_{2\text{a}}K_{2\text{b}}(\text{O}_2)_v} = \frac{k_{2\text{bf}}K_{2\text{a}}}{2k_{1[\text{O}^*-\text{*}]}(\text{CH}_4)} \left(\frac{\text{O}_2}{\text{CH}_4} \right) \quad (18a)$$

$$(\text{O}_2)_v = \frac{k_{2\text{bf}}k_{2\text{br}}K_{2\text{a}}}{4k_{1[\text{O}^*-\text{*}]}^2} \left(\frac{\text{O}_2}{\text{CH}_4} \right)^2 \quad (18b)$$

These $(\text{O}^*)/(\text{*})$ and $(\text{O}_2)_v$ values in regime 2 are single-valued functions of the O_2/CH_4 ratio and not just of O_2 pressure as in

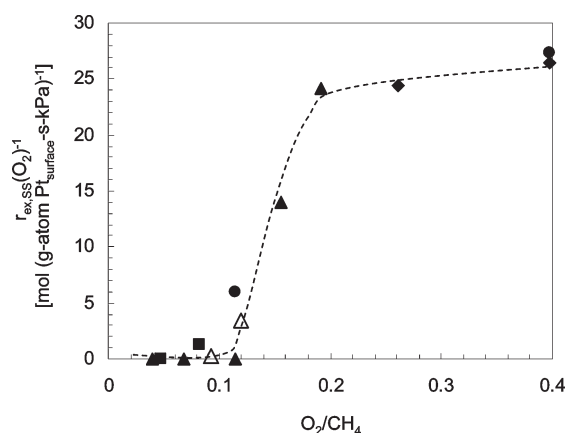


Figure 8. Pseudo first-order oxygen-exchange rate constants ($r_{\text{ex,ss}}(\text{O}_2)^{-1}$, 873 K) during $\text{CH}_4\text{-}^{16}\text{O}_2\text{-}^{18}\text{O}_2$ reactions on Pt clusters (8.5 nm average cluster size) for 0.6 kPa (\blacklozenge), 1.2 kPa (\bullet), 2.4 kPa (\blacktriangle), 3.6 kPa (\triangle), and 4.8 kPa (\blacksquare) CH_4 plotted against the O_2/CH_4 reactant ratio. (0.15 mg 0.2% wt Pt/ Al_2O_3 , 200 SiO₂/catalyst intraparticle (λ) and 4700 quartz/catalyst interparticle (χ) dilution ratios, 2.08 cm³ (STP) s⁻¹, $^{16}\text{O}_2/^{18}\text{O}_2 = 1$).

regime 1 (section 3.2). At any given O_2 pressure, $(\text{O}^*)/(\ast)$ values in regime 2 are smaller than those at chemical equilibrium and, by inference, $(\text{O}_2)_v$ are smaller than the prevalent O_2 pressures, because of more effective O^* scavenging by CH_4 reactions in this regime. These lower $(\text{O}_2)_v$ and oxygen chemical potentials reduce the oxidation tendencies of Pt clusters from those given by the actual O_2 pressures. Oxygen chemical potentials are lower in this regime than in regime 1; thus, the bulk of the Pt clusters remains in the metallic phase.

The ratio of $^{16}\text{O}_2\text{-}^{18}\text{O}_2$ exchange rate constants during steady-state catalysis (in $\text{CH}_4\text{-}^{18}\text{O}_2\text{-}^{16}\text{O}_2$ mixtures) to those at chemical equilibrium (in $^{18}\text{O}_2\text{-}^{16}\text{O}_2$ mixtures) (χ_2) provides otherwise inaccessible estimates of O^* coverages and $(\text{O}_2)_v$ values (eqs 18a–18b) during steady-state $\text{CH}_4\text{-O}_2$ reactions relative to those at chemical equilibrium with the prevalent O_2 pressures. Figure 5 shows the effective rate constants for O_2 isotopic exchange ($r_{\text{ex,2}}(\text{O}_2)^{-0.5}$; eq 6b) for $\text{CH}_4\text{-}^{16}\text{O}_2\text{-}^{18}\text{O}_2$ reactions in regime 2 ($0.08 < \text{O}_2/\text{CH}_4 < 2$; 8.5 nm Pt clusters) together with their measured values in regime 1 ($\text{O}_2/\text{CH}_4 > 2$; 8.5 nm Pt clusters) and also with the values measured in $^{18}\text{O}_2\text{-}^{16}\text{O}_2$ mixtures without CH_4 . O_2 exchange rate constants in regime 2 decreased with decreasing O_2/CH_4 ratio and become smaller than those in regime 1 ($16.5 \text{ mol (g-atom Pt}_{\text{surface-s}})^{-1} \text{ kPa}^{-0.5}$), which equal those at chemical equilibrium (section 3.2). The ratios of these rate constants to those at equilibrium (χ_2) are near unity in regime 1, but decrease as $\text{CH}_4\text{-O}_2$ reactions undergo a transition from regime 1 to 2 and as the faster C–H activation steps on $\text{O}^*\text{-}\ast$ site pairs deplete the O^* and prevent oxygen equilibration. The O_2 exchange rate equation (eq 6b), derived by assuming equilibrated O_2 dissociation steps, becomes inadequate to describe the $^{16}\text{O}_2\text{-}^{18}\text{O}_2$ rate dependence in this regime. This is shown in Figure 5 where the O_2 exchange “rate constants” ($r_{\text{ex}}(\text{O}_2)^{-0.5}$) are no longer constant, but decrease with decreasing O_2/CH_4 ratio. The exchange rates remain proportional to O^* and O_2^* concentrations, the latter of which are proportional to the O_2 pressures and the number of binding sites (\ast). As a result, the pseudo first-order O_2 exchange rate constants ($r_{\text{ex,ss}}(\text{O}_2)^{-1}$) are proportional to the O^* and \ast concentrations, similar to the case for CH_4 conversion in this regime ($r_2(\text{CH}_4)^{-1}$)

because both steps use the $\text{O}^*\text{-}\ast$ pairs. Thus, $r_{\text{ex,ss}}(\text{O}_2)^{-1}$ values are also a strict function of O_2/CH_4 ratios and of the related O^* coverages and $(\text{O}_2)_v$, as shown in Figure 8.

We analyze next the elementary steps involved in O_2 adsorption (Step 2.1) and C–H and $\text{O}=\text{O}$ bond dissociation steps (Steps 1.2 and 2.2) that control reactivities in regime 2 by carrying out DFT calculations over different $\text{O}^*\text{-}\ast$ site pairs on O^* -covered Pt_{201} clusters. More specifically, we analyze the activation and reaction energies to determine the most favorable $\text{O}^*\text{-}\ast$ sites for CH_4 activation on the (111) terrace which comprises a central terrace oxygen vacancy site (\ast) (type 4, Scheme 1) and a reactive next nearest-neighbor O^* site. O^* chemisorbed at site IV is the only active site because the nearest-neighbor O^* sites (site V) are too close to the adsorbed CH_4 at that site. This results in very high repulsive interactions and barriers that exceed 170 kJ mol^{-1} . We examine the C–H bond activation on $\text{O}^*\text{-}\ast$ site pairs in the high O_2/CH_4 region (>0.25) where \ast presents as an isolated species and then extend our study to lower O_2/CH_4 ratios (<0.25) at which the $\text{O}^*\text{-}\ast$ sites and vicinal \ast species form larger ensembles that may influence the C–H bond activation barriers.

Calculations were carried out on isolated O^* vacancies (also exposed Pt atoms) at (111) facets of O^* covered Pt_{201} clusters (O^* occupies all of the other (111) fcc and (100) bridge sites). O^* coverages ($\text{O}^*/\text{O}^*_{\text{max}}$) are >0.99 , consistent with the mechanistic proposal of O^* as MASI required to describe rate data with the presence of isolated vacancies. The structures of the reactants, transition states, and products of C–H bond activation on $\text{O}^*\text{-}\ast$ site pairs are shown in Figure 9. C–H bond activation occurs via concerted oxidative addition⁸² of the exposed Pt atom to C–H bonds and H-abstraction by O^* with a barrier of 144 kJ mol^{-1} . The transition state is stabilized by both C and H interactions with the exposed Pt atom which is evident from the elongation of the C–H bond. This elongation lowers the C–H antibonding ($\sigma^*_{\text{C-H}}$) orbital, thus allowing for the back-donation of electron density from the metal into this state and dissociation of the C–H bond (Pt–C and Pt–H bond lengths at the transition state are 0.234 and 0.208 nm, respectively). The O^* atom, initially adsorbed at the threefold fcc site, migrates to the bridge position to interact with the H in CH_4 (O–H bond is 0.149 nm at the transition state) and assist in the C–H bond activation. This step occurs together with the metal insertion into the C–H bond to form a four-centered ($\ast\text{-CH}_3\text{-H-O}^*$)[‡] transition state (Figure 9b), in a process reminiscent of σ -bond metathesis and 1,2 addition on organometallic complexes, which form (M–C–H–X)[‡] transition states (M = metal, X = amido, alkoxo, imido, etc.).^{83–85} These findings confirm the synergistic roles of \ast and O^* in C–H bond activation, in which vacancies weaken C–H bonds and stabilize the CH_3 fragment and O^* abstract and stabilize the H-atom. These conclusions suggest that $\text{O}^*\text{-}\ast$ site pairs in which \ast can form strong $\ast\text{-CH}_3$ bonds but O^* are weakly bound would give the most stable transition states and the lowest C–H bond activation barriers.

The specific influence of the properties of O^* and \ast sites on C–H bond activation barriers was probed by varying O^* and $\ast\text{-CH}_3$ binding energies. O^* binding energy effects were explored by varying O^* coverages and binding energies on extended Pt(111) surfaces with surface Pt atoms of identical coordination and similar in structure to the (111) facets in large Pt clusters. As O^* coverage increases (from 0.11 to 0.67 ML), the O^* binding energy (expressed here as heat of atomic oxygen adsorption, Q_{O^*}) decreases (from 256 to 365 kJ mol^{-1});⁸⁶ C–H bond activation barriers decrease linearly from 122 to 94 kJ mol^{-1} (see Supporting

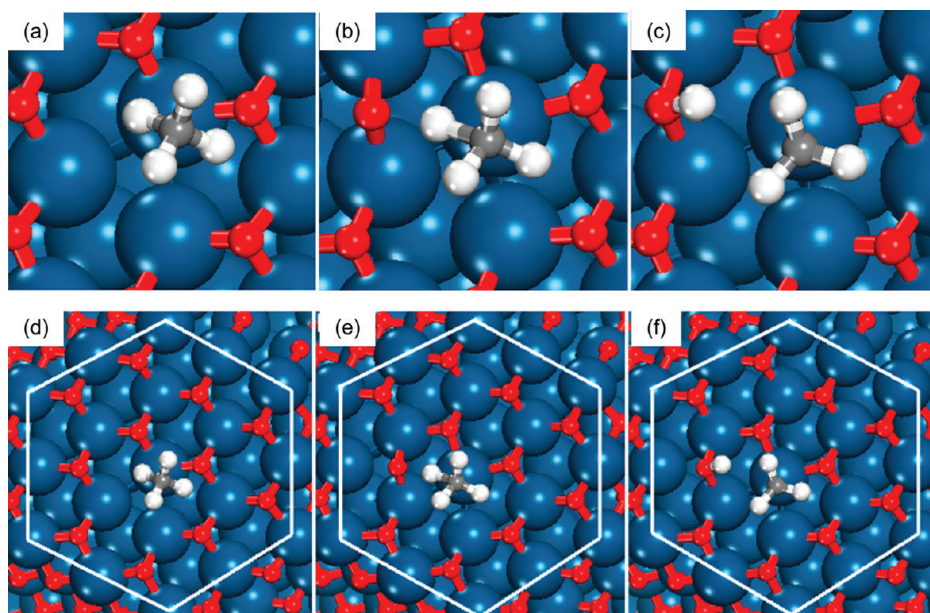


Figure 9. Structures of reactant (a,d) ($\text{CH}_4(\text{g}), \text{O}^*-\text{*}$), transition (b,e) $\{(\text{H}_3\text{C}^*-\text{*OH})^\ddagger\}$, and product (c,f) ($\text{CH}_3^*, \text{OH}^*$) states for the initial C–H bond dissociation in CH_4 on $\text{O}^*-\text{*}$ site pairs formed from an O^* atom (site IV, Scheme 1) and a Pt atom (site 4, Scheme 1) on the (111) facet of a Pt_{201} cluster nearly saturated with chemisorbed oxygen atoms ($\text{O}^*/\text{O}_{\text{max}} = 0.99$). O–H, C–H, and Pt–C bond lengths of the $(\text{*}-\text{CH}_3-\text{*OH})^\ddagger$ transition state complex are 0.149 nm, 0.128 nm, and 0.234 nm, respectively. (See Supporting Information Figure S-2 for the view of the entire Pt cluster.)

Information Figures S-3 and S-4) with increasing O^* coverage and decreasing O^* binding energy, consistent with Brønsted-Evans-Polanyi (BEP) relations and with similar trends reported for C–H activation in CH_3OCH_3 on $\text{O}^*-\text{*}$ site pairs on Pt⁴⁴ and also in accordance with proposed basis for the high reactivity of weakly bound O^* on Ag.⁸⁷ The effects of M– CH_3 binding energies on C–H bond activation rates were examined by varying the coordination number of the * site in $\text{O}^*-\text{*}$ site pair on Pt_{201} clusters. These effects of Pt coordination number on C–H bond activation barriers were recently examined for $\text{O}^*-\text{*}$ site pairs on bare Pt_{201} clusters and reported elsewhere.²⁶ C–H bond activation barriers on $\text{O}^*-\text{*}$ site pairs were found to decrease from 119 kJ mol^{-1} to 88 kJ mol^{-1} as the coordination number of the * site in the $\text{O}^*-\text{*}$ site pair decreases from 9 to 6 and the M– CH_3 bond strength concomitantly increases.²⁶ On coordinatively unsaturated sites such as corner and edge sites (sites 1 and 2 in Scheme 1, respectively), the barriers were lower because these sites afford stronger Pt–C interactions and concomitantly higher reaction exothermicity, consistent with the predicted trend between barriers and heats of reaction from the BEP relation. Similar trends between barriers and heats of reaction and the related metal–carbon binding energies were also reported for C–H bond activation on the $\text{*}-\text{*}$ site pairs on Pt_{201} clusters²⁶ and on closed-packed metal surfaces,⁸⁸ because C–H bond activation steps on both the $\text{O}^*-\text{*}$ and $\text{*}-\text{*}$ site pairs occur via oxidative addition of the metal atom to the C–H bond.²⁶ These trends were also found for $\text{*}-\text{*}$ site pairs on closed-packed surfaces of different metals, in which the barriers decrease from 200 kJ mol^{-1} to 71 kJ mol^{-1} as the M– CH_3 bond strength increases from 115 kJ mol^{-1} (Au(111)) to 253 kJ mol^{-1} (Rh(111)), respectively.⁸⁹

The effective barrier for methane activation in regime 2 (eq 13) includes contributions from CH_4 ($E_{1[\text{O}^*-\text{*}]}$) and oxygen activation barriers ($E_{2\text{bf}} - Q_{\text{O}_2}$), each of which is given by the difference in energy between the transition state ($(\text{*}-\text{CH}_3-\text{*H}-\text{O}^*)^\ddagger$ or

$(\text{O}^*=\text{*O})^\ddagger$) and its gas-phase reactants (CH_4 or O_2) as their adsorption from the gas phase is quasi-equilibrated. The CH_4 activation barrier on a single isolated vacancy with a vicinal O^* is 144 kJ mol^{-1} . O_2 , however, cannot directly dissociate to form 2O^* on an isolated vacancy (*). Instead, it adsorbs as O_2^* in equilibrated steps (Step 2.1) and then dissociates onto a vicinal O^* site resulting in the formation of a new O_2^* ($^x\text{O}_2^* + ^y\text{O}^* \rightarrow ^x\text{O}^* + ^x\text{O}^y\text{O}^*$; x and y are used to differentiate the O^* ; Step 11). This process of O_2^* activation by vicinal O^* allows for the rapid migration of O^* along the top of the O^* -covered surface, which continues until O_2^* finds a vacancy site and dissociates via the reaction $\text{O}_2^* + \text{*} \rightarrow 2\text{O}^*$ (Step 2.2) to complete the O_2 dissociation process. Such mobile O^* species and elementary steps have also been proposed to account for O_2 activation during isotopic exchange and NO– O_2 reactions on Pt and Pd surfaces.^{61,90}

The reaction energy diagram for O_2 activation at isolated vacancies on Pt clusters (Figure 10a) includes the initial formation of weakly coordinated η_1 -superoxo O_2^- intermediate with a barrier of 58 kJ mol^{-1} , which contrasts the barrierless adsorption of O_2 at low O^* coverages ($\text{O}^*/\text{O}_{\text{max}}^* = 0.01$) on Pt_{201} clusters involving the exothermic formation of η_2 -peroxo species (section 3.4). O_2 adsorption cannot occur in a η_2 configuration on Pt cluster surfaces at near O^* saturation in the absence of $\text{*}-\text{*}$ ensembles. O-atoms instead migrate on top of the O^* covered surface via the formation of three-centered $(^x\text{O}-^x\text{O}^y\text{O})^\ddagger$ transition states in which the O-atom in O_2^* that is not in contact with the surface ($\text{O}_{\text{migrating}}$) is shared between the bound oxygen of O_2^* ($\text{O}_{\text{bound}}^*$) and the vicinal O^* ($\text{O}_{\text{vicinal}}^*$), as shown in Figure 10a. The barrier for this O-atom transfer step is 75 kJ mol^{-1} . O^* migration continues until the newly formed O_2^* resides next to a vacancy site (*), a situation that causes dissociation via a late transition state in which the migrating oxygen ($\text{O}_{\text{migrating}}$) binds with the exposed metal atom. This step exhibits the largest barrier (207 kJ mol^{-1}) compared with the barriers for molecular O_2 adsorption (58 kJ mol^{-1}), O^* migration (75 kJ mol^{-1}), and O_2

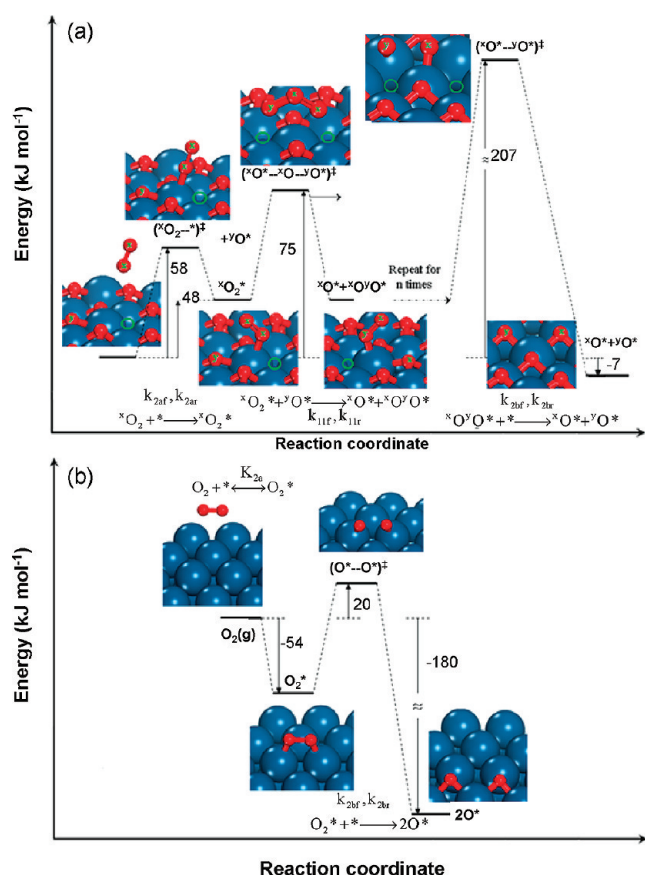


Figure 10. (a) Reaction coordinate and structures of reactant, transition state, intermediate, and product for O₂ dissociation on the (111) facet of a Pt₂₀₁ cluster nearly saturated with chemisorbed oxygen atoms where oxygen vacancies present as isolated species (O^{*}/O_{max} = 0.99) (Green circle denotes oxygen vacancy; *x* and *y* are used to differentiate the O atoms involved in the steps). (b) Reaction coordinate and structures of reactant, transition state, and product for O₂ dissociation on the (111) facet of a bare Pt₂₀₁ cluster. (Refer to Scheme 2 for the elementary reaction steps and rate constants.)

desorption (10 kJ mol⁻¹). Thus, the elementary O₂* dissociation step is irreversible and is kinetically relevant while O₂ adsorption and O migration steps are quasi-equilibrated. The effective rate constant for O₂ dissociation ($k_{\text{eff},\text{O}_2}$) is then given by

$$k_{\text{eff},\text{O}_2} = k_{2\text{bf}}K_{2\text{a}}K_{11} = k_{2\text{bf}}K_{2\text{a}} \quad (19)$$

in terms of the O₂ dissociation rate constant ($k_{2\text{bf}}$) and the O₂* adsorption ($K_{2\text{a}}$) and O atom migration (K_{11}) equilibrium constants (Scheme 2, Figure 10a for the definition of these constants). The O* migration equilibrium constant (K_{11}) equals unity because the free energy change for this step is zero. Thus, the effective O₂ dissociation rate constant (eq 19) is equal to the product of O₂* adsorption equilibrium constant and O₂* dissociation rate constant, $k_{2\text{bf}}K_{2\text{a}}$, used in eqs 9 and 11. The rate expression is identical to the one derived by assuming direct O₂ dissociation steps occur over two vacancy sites but contains different kinetic requirements and reflects different O₂ activation paths.

DFT-derived barriers for C–H bond (144 kJ mol⁻¹) and O₂ (207 kJ mol⁻¹) activation can be used together with eq 11 to estimate an effective barrier of 81 kJ mol⁻¹ for kinetic regime 2, in excellent agreement with measured activation energies (79 kJ mol⁻¹; Table 1). These barriers are much smaller than for CH₄ activation

on O*–O* site pair in regime 1 (155 kJ mol⁻¹ (experiment) and 149 kJ mol⁻¹ (theory)), consistent with the much higher CH₄–O₂ chemical conversion rates in regime 2 than regime 1. Although the calculated effective barrier in regimes 2 is in very good agreement with measured barriers, the intrinsic C–H (144 kJ mol⁻¹) activation barrier in this regime is higher than expected and is rather similar to that in regime 1 (149 kJ mol⁻¹), especially considering the significant differences in rates between these two regimes. It is likely that the intrinsic barrier for O₂ dissociation (207 kJ mol⁻¹) is also higher than expected. The high C–H bond activation barriers are likely due to the fact that the isolated Pt site vacancies are not fully exposed and therefore cannot take full advantage of the formation of a strong M–CH₃ bond in the transition state because O* atoms on the surface appear to block access to the vacancy site. This may be the result of the constraints imposed by not considering the changes that occur in the adlayer structure prevalent at the high temperatures and O₂ pressures of this reaction. Including these effects would likely increase oxygen saturation coverages and further expand the lattice which will help to push the metal atoms out of the surface and thus better expose the vacancy sites. We have seen similar effects on Pt(111) surfaces where saturation surface coverages result in a buckling of the surface structure which exposes metal sites (see Supporting Information Figure S-4) and lowers the barrier from 122 kJ mol⁻¹ at 0.25 O* ML to 94 kJ mol⁻¹ at 0.67 O* ML. The buckling of surfaces is consistent with the formation of 2D oxide chains on O*-covered Pt(111) surfaces⁹¹ and the stronger O* adsorption at step edges of the Ag(*n*10) (*n* = 2, 4) surfaces.⁹² We will report these details in surface reconstruction and their influence on both the C–H and O=O activation barriers in a followup manuscript. The over prediction of the C–H and O₂ dissociation barriers appear to cancel one another out in determining the effective activation energy barrier (eq 11), as both are limited by the exposure and access to metal vacancy sites in the fully covered O*-adlayer. Similar cancelations in C–H and O₂ dissociation barriers are also likely to occur in the low O₂/CH₄ region of regime 2.

As O₂/CH₄ ratios decrease, O* coverages decrease, and the vacancy concentration increases (eq 18a) and ultimately lead to vicinal *–* sites; these trends also cause an increase in the O* binding strength near such sites and a concomitant decrease in the reactivity of O* in H-abstraction. Yet, C–H bond activation barriers decreased from 144 kJ mol⁻¹ to 125 kJ mol⁻¹ and to 70 kJ mol⁻¹ as the number of oxygen vacancies increased from 1 to 3. Larger ensembles of vacancies reflect a decrease in the number of O* bound to each exposed Pt atom and, in turn, stronger interactions between CH₄ and exposed Pt atoms. These interactions stabilize the C–H bond activation transition states and compensate for the lower O* reactivity caused by the increase in O* binding strength.

3.4. Kinetically Relevant O=O Activation on Pt Surfaces Uncovered of Oxygen Atoms (Kinetic Regime 3). Turnover rates for CH₄–O₂ ultimately decrease as the size of the oxygen vacancy ensemble increases with decreasing O₂/CH₄ ratios beyond those that define kinetic regime 2 (O₂/CH₄ < 0.08, 873 K, 8.5 nm clusters, Figures 2 and 3). This transition in rate dependence reflects a decrease in oxygen chemical potential and O* coverage, which causes O*-mediated C–H bond activation to become less frequent and rates ultimately to become limited by O₂ activation. In this regime (denoted regime 3 in Figures 2 and 3), rates become proportional to O₂ pressure and independent of CH₄ pressure. We rule out mass transport across boundary layers

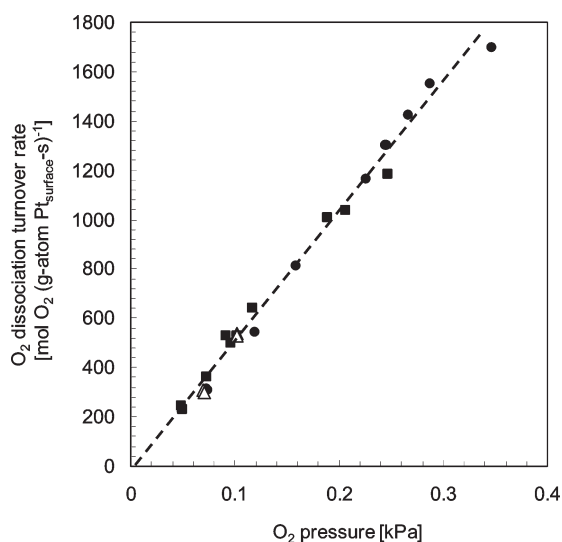


Figure 11. O₂ dissociation turnover rates (873 K) during CH₄–O₂ (●), CD₄–O₂ (△), and CO–O₂ (■) reactions on Pt clusters (8.5 nm average cluster size) measured in kinetic regime 3 ($0 < \text{O}_2/\text{CH}_4 < 0.08$), in which O₂ dissociation is the sole kinetically relevant step (Step 2.2, Scheme 2). (0.15 mg 0.2% wt Pt/Al₂O₃, 4.9 kPa CH₄, 4.9 kPa CD₄, or 0.5–0.65 kPa CO, 200 SiO₂/catalyst intraparticle (λ) and 4700 quartz/catalyst interparticle (χ) dilution ratios, 2.08 cm³ (STP) s⁻¹).

around catalyst pellets (which would give such a rate dependence) as the controlling step by varying intrapellet dilution ratios from 100 to 300 without consequences on measured rates, as reported elsewhere.²⁶ The measured first-order dependence on O₂ indicates that rates are limited solely by the reactive collisions of O₂ on essentially bare Pt cluster surfaces. CH₄ turnover rates in this regime are given by

$$r_3 = 0.5K_{2a}k_{2bf}(\text{O}_2) \quad (20)$$

In this regime, C–H bond activation becomes kinetically irrelevant, consistent with the absence of CH₄/CD₄ kinetic isotope effects (KIE, 1.0 ± 0.15 , Table 1, Figure 11). The sole kinetic relevance of the O₂ dissociation step (Step 2.2, Scheme 2) is also consistent with turnover rates that do not depend on reductant pressures for both CO–O₂ and CH₄–O₂ reactions at the conditions required for this regime (0.05–0.35 kPa O₂, 873 K, Figure 11). The O₂ consumption rates in CO–O₂ and CH₄–O₂ mixtures, which are related to the CO or CH₄ turnover rates via the respective reaction stoichiometries, are essentially identical at each O₂ pressure, because these reactions are limited by the same O₂ dissociation step on surfaces essentially free of adsorbed species.

Turnover rates at all O₂ pressures in regime 3 are much larger than for C–H bond activation steps in CH₄–H₂O/CO₂ mixtures (regime 4) when comparing the rates at a given CH₄ pressure (<5 kPa). Thus, it appears that C–H bond activation occurs much more rapidly with CH₄–O₂ than with CH₄–H₂O reactants, because otherwise, CH₄–O₂ reaction rates would be limited by C–H bond activation instead of O₂ dissociations steps and equal to those in CH₄–H₂O mixtures. C–H bond activation rate constants measured at low O* coverages in ¹³CH₄–¹²CO–O₂ mixtures remain insensitive to O* content; thus, the C–H bond activation step must also occur predominantly on *–* site pairs that are prevalent in

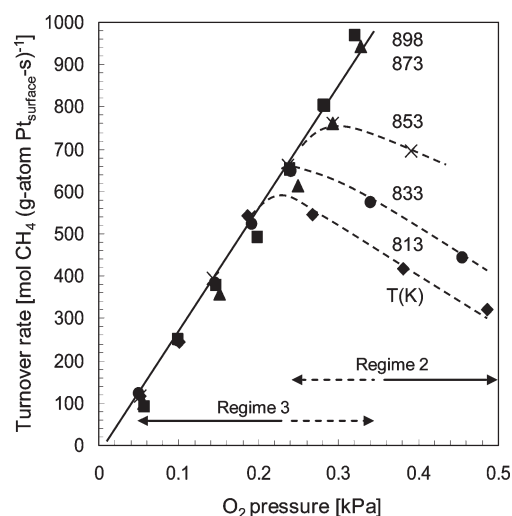


Figure 12. Effects of O₂ pressure on CH₄ turnover rates during CH₄–O₂ reactions at 813 K (◆), 833 K (●), 853 K (×), 873 K (▲), and 898 K (■) in regimes 2 (---, dashed line) and 3 (—, solid line) on Pt clusters (8.5 nm average cluster size). (0.15 mg 0.2% wt Pt/Al₂O₃, 4.9 kPa CH₄, 200 SiO₂/catalyst intraparticle (λ) and 4700 quartz/catalyst interparticle (χ) dilution ratios, 2.08 cm³ (STP) s⁻¹).

this regime.²⁶ Although the CH₄ activation proceeds via the same kinetically relevant step on *–* site pairs, rates were much larger in CH₄–O₂ (regime 3) than in CH₄–H₂O/CO₂ (regime 4) mixtures. We surmise that a portion of the coordinatively unsaturated sites that are highly effective for C–H bond activation⁷ are occupied by the products of CH₄ activation (CH_x*) in CH₄–H₂O/CO₂ reactions; these sites do not participate in turnovers and remain kinetically invisible at all H₂O/CH₄ or CO₂/CH₄ ratios in regime 4. These undercoordinated sites, however, become available for catalytic turnovers in CH₄–O₂ mixtures because CH_x* are removed by reactions with O*.²⁶

Rate constants for CH₄ conversion in regime 3 (eq 20) are related to O₂ dissociation rate constant ($K_{2a}k_{2bf}$, $5.6 \times 10^3 \pm 195 \text{ kPa}^{-1} \text{ s}^{-1}$, 873 K, Table 1) by the stoichiometry of the combustion reaction. O₂ dissociation rate constants reflect the rate of O₂ collisions with Pt cluster surfaces and a sticking coefficient, which is found to be $\sim 3.5 \times 10^{-3}$, similar to values reported on Pt(111) (0.016; extrapolated to 873 K from sticking coefficients measured at 320–620 K).⁹³ The measured barrier for O₂ dissociation ($E_{2bf} - Q_{\text{O}_2}$) reflects the difference between the O₂* dissociation activation barrier (E_{2bf}) and the heat of molecular O₂ adsorption (Q_{O_2}). The O₂ dissociation barrier on uncovered surfaces is typically small, unlike those on surfaces nearly saturated with O* (Figure 10a), as confirmed by DFT-derived values reported below. Measured rates depend weakly on temperature (810–900 K, Figure 12) and measured activation energies were near zero ($\sim 3 \text{ kJ mol}^{-1}$) and much smaller than in regimes 1, 2, and 4 (155 kJ mol⁻¹, 79 kJ mol⁻¹, and 75–(H₂O)–83(CO₂) kJ mol⁻¹, respectively), where barriers reflect those for C–H bond activation steps ($E_{1[\text{O}^*-\text{O}^*]}$, $E_{1[\text{O}^*-\text{O}^*]}$ (eq 13), or $E_{1[\text{O}^*-\text{O}^*]}$; Table 1). The measured pre-exponential factor ($5.6 \times 10^3 \pm 200 \text{ kPa}^{-1} \text{ s}^{-1}$ (per O₂ molecule turnover), 873 K, Table 1) in regime 3 is larger than estimates derived from a transition state formalism by assuming an immobile activated structure ($5.5 \times 10^1 \text{ kPa}^{-1} \text{ s}^{-1}$)⁹⁴ and reflects an entropy loss between the reactant and transition state of $-125.5 \text{ J mol}^{-1} \text{ K}^{-1}$.

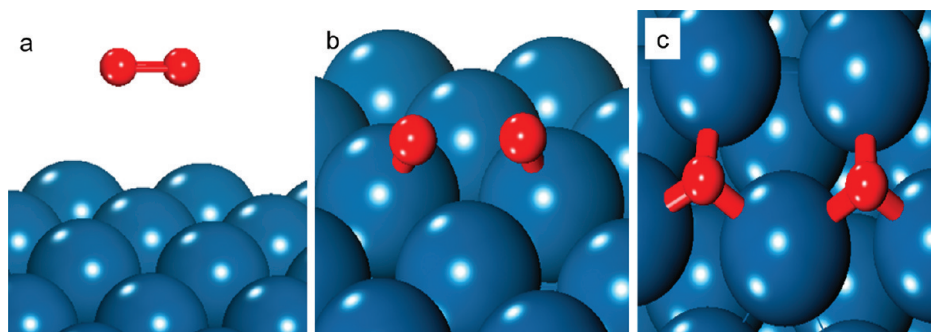


Figure 13. Structures of reactant (a, $\text{O}_2(\text{g})$), transition state (b, $(\text{*O--O})^\ddagger$), and product (c, 2O^*) during O_2 dissociation (Steps 2.1 and 2.2, Scheme 2) on a Pt_{201} cluster surface uncovered of reactive intermediates. The $(\text{O--O})^\ddagger$ bond length at the transition state is 0.184 nm. The reaction coordinate is shown in Figure 10b.

DFT treatments were used to describe the molecular details of kinetically relevant O_2 dissociation steps on bare Pt_{201} clusters, as shown in Figure 10b. O_2 molecular adsorption (Step 2.1) requires a triplet-to-singlet transition upon adsorption, as also found for O_2 adsorption on CO-covered Pt(111) and Pt_{201} cluster surfaces.^{95,96} O_2^* prefers to adsorb in a di- σ configuration (Figure 13), as a molecular precursor to O_2^* dissociation (Step 2.2), as shown previously.⁹⁷ O_2^* dissociation (Step 2.2) occurs over a Pt atom that connects the two neighboring threefold fcc sites that ultimately bind the O^* products via a late transition state (Figure 13b) at which the $\text{O}=\text{O}$ bond lengthens from 0.124 nm in $\text{O}_2(\text{g})$ to 0.176 nm. There is a charge transfer from the metal into the antibonding $2\pi^*$ state in O_2 that occurs upon the adsorption of O_2 to the surface. The two O^* atoms formed bind to vicinal threefold fcc sites with $\text{O}-\text{Pt}$ bonds about 0.210 nm in length and share a Pt atom. The effective barrier ($E_{2\text{bf}} - Q_{\text{O}_2}$) for O_2 dissociation, measured as the difference in energy between the $(\text{*O--O})^\ddagger$ transition state and $\text{O}_2(\text{g})$, is $<20 \text{ kJ} (\text{mol O}_2)^{-1}$, consistent with the measured barriers ($<3 \text{ kJ mol}^{-1}$). The barrier is much smaller than on O^* -saturated Pt_{201} clusters (207 kJ mol^{-1}), because repulsive interactions among O^* atoms are absent on bare surfaces; the differences in structures and energetics of the O_2 activation steps on bare and O^* covered Pt cluster surfaces are shown in Figure 10. The nearly cleaved $\text{O}=\text{O}$ bonds and the nearly formed $\text{O}-\text{Pt}$ bonds (0.199 and 0.201 nm) at the late transition states are consistent with the large entropic losses (Table 1) detected in the rate measurements.

3.5. Effects of Temperature on O^* Coverage and Consequences for the O_2/CH_4 Ratios Required for Transitions among Kinetic Regimes. The O_2 pressures and O_2/CH_4 ratios required to attain the O^* coverages that lead to transitions among regimes depend on temperature, because the rate and equilibrium constants in eqs 5 and 18a and 18b vary with temperature. Figure 12 shows that CH_4 turnover rates increased and then decreased with increasing O_2/CH_4 ratio for temperatures between 813 and 898 K, consistent with the mechanistic conclusions reached based on kinetic and isotopic studies at 873 K and discussed above. The transition from bare (regime 3) to O^* -covered (regime 2) Pt clusters occurs near the O_2/CH_4 ratio required for maximum rates, which increases with increasing temperature (from 0.045 at 813 K to 0.06 at 853 K). Simplifying eq 15 with the assumptions that C-H bonds are predominantly activated on $\text{O}^*-\text{*}$ and $\text{*}-\text{*}$ site pairs and the rates of O^* removal via recombination are much smaller than their reactions with

CH_4 (section 3.3) leads to steady-state $[(\text{O}^*)/(\text{*})]_{\text{ss}}$ ratios in regimes 2 and 3

$$\frac{[(\text{O}^*)]}{(\text{*})}_{\text{ss, 2\&3}} = \frac{k_{2\text{bf}}K_{2\text{a}}}{2k_{1[\text{O}^*-\text{*}]}} \frac{(\text{O}_2)}{(\text{CH}_4)} - \frac{k_{1[\text{*}-\text{*}]}}{k_{1[\text{O}^*-\text{*}]}} \quad (21)$$

which depends on O_2/CH_4 ratios and on rate ($k_{2\text{bf}}$, $k_{1[\text{O}^*-\text{*}]}$, $k_{1[\text{*}-\text{*}]}$) and thermodynamic ($K_{2\text{a}}$) constants and, in turn, on the effective barriers for O_2^* ($E_{2\text{bf}}$) and CH_4 ($E_{1[\text{O}^*-\text{*}]}$, $E_{1[\text{*}-\text{*}]}$) dissociation, the heat of molecular O_2 adsorption (Q_{O_2}), and the pre-exponential factors (A_i) for the elementary step i in Scheme 2

$$\frac{[(\text{O}^*)]}{(\text{*})}_{\text{ss, 2\&3}} = \frac{A_{2\text{bf}}A_{2\text{af}}}{2A_{1[\text{O}^*-\text{*}]}A_{2\text{ar}}} \exp\left[\frac{-(E_{2\text{bf}} - Q_{\text{O}_2} - E_{1[\text{O}^*-\text{*}]})}{k_{\text{B}}T}\right] \left(\frac{\text{O}_2}{\text{CH}_4}\right) - \frac{A_{1[\text{*}-\text{*}]}}{A_{1[\text{O}^*-\text{*}]}} \exp\left[\frac{-(E_{1[\text{*}-\text{*}]} - E_{1[\text{O}^*-\text{*}]})}{k_{\text{B}}T}\right] \quad (22)$$

The pre-exponential factors ($A_{2\text{af}}$, $A_{2\text{ar}}$, $A_{2\text{bf}}$, $A_{1[\text{O}^*-\text{*}]}$, $A_{1[\text{*}-\text{*}]}$) vary weakly with temperature (e.g., $\sim T^{-0.5}$ for an immobile transition state complex⁹⁴). Both of the exponential terms, however, decrease dramatically with increasing temperature, because the barriers for C-H bond dissociation on $\text{O}^*-\text{*}$ site pairs at low O^* coverages ($E_{1[\text{O}^*-\text{*}]}$, 91–121 kJ mol^{-1} for 0.01 ML on Pt_{201} clusters²⁶) are much larger than on $\text{*}-\text{*}$ site pairs ($E_{1[\text{*}-\text{*}]}$, 89 kJ mol^{-1} on Pt(111) and 50–82 kJ mol^{-1} on Pt_{201} clusters²⁶) and those for O_2 dissociation ($E_{2\text{bf}} - Q_{\text{O}_2}$, $<3 \text{ kJ mol}^{-1}$ (experimental) and $\sim 20 \text{ kJ mol}^{-1}$ (theory)). Thus, $(\text{O}^*)/(\text{*})$ ratios for any given O_2/CH_4 value are lower at higher temperatures and reactions occur on uncovered surfaces (regime 3) over a wider operating O_2/CH_4 window.

3.6. Effects of Pt Cluster Size and Oxygen Binding Strength on CH_4 Conversion Rates. The specific effects of Pt cluster size on turnover rates differ among the kinetic regimes discussed here, because each regime reflects rate and equilibrium constants with potentially different sensitivity to the coordination of exposed metal atoms, which vary with cluster size. We examine the consequences of Pt cluster size and of the coordination and binding properties of exposed Pt atoms on rates in each regime. The effects of cluster size were measured on a series of 0.2% wt Pt/ Al_2O_3 catalysts at 873 K and the data are shown in Figure 14 and Table 3.

The $\text{*}-\text{*}$ site pairs on small clusters predominantly consist of coordinatively unsaturated atoms, which bind CH_3^* and H^* strongly in stabilizing the C-H bond activation transition state, $(\text{*}-\text{CH}_3-\text{H}-\text{*})^\ddagger$, during $\text{CH}_4-\text{H}_2\text{O}/\text{CO}_2$ reactions (regime 4).²⁶

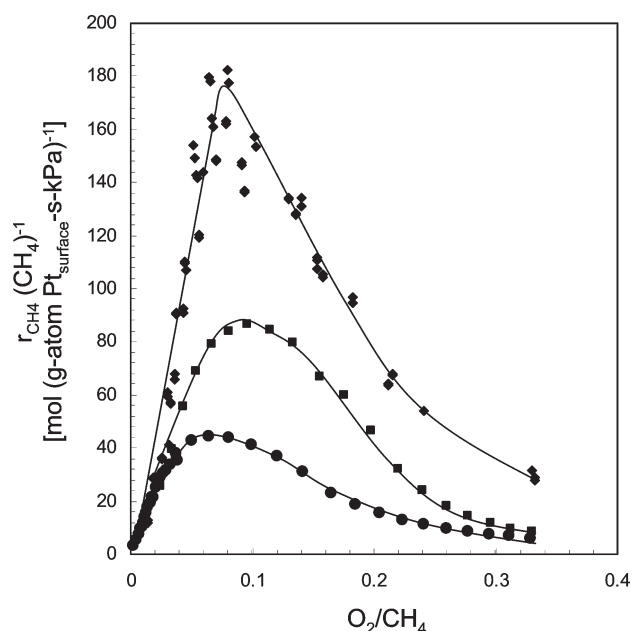


Figure 14. Generalized correlation of pseudo first-order rate constants, $r(\text{CH}_4)^{-1}$, and O_2/CH_4 ratio during $\text{CH}_4\text{--O}_2$ reactions on supported Pt clusters of different sizes (1.8 nm (●), 3.3 nm (■), and 8.5 nm (◆) average cluster sizes) in kinetic regimes 2 and 3. (0.15 mg 0.2% wt Pt/ Al_2O_3 , 200 SiO_2 /catalyst intraparticle (λ) and 4700 quartz/catalyst interparticle (χ) dilution ratios, 2.08 cm^3 (STP) s^{-1}).

Strong binding of CH_3^* and H^* leads to more exothermic reactions and stabilizes transition states to give smaller activation barriers, consistent with thermodynamic guidance from Brønsted-Evans-Polanyi (BEP) relations.²⁶ This decrease in C–H bond activation barriers caused the larger rates widely reported for reforming reactions on smaller clusters of Pt (Table 1) and of other Group VIII metals.^{6,8–11}

C–H bond dissociation rates on $\text{O}^*\text{--O}^*$ site pairs (regime 1) exhibit instead an opposite effect of cluster size. Measured rate constants ($k_{1[\text{O}^*\text{--O}^*]}$, Step 1.1) increased by a factor of ~ 2.5 as Pt cluster size increased from 1.8 to 8.5 nm. The barrier for this step depends on the energy required to promote the O^* to the active bridge sites and to interact with the H (section 3.2). O^* binding energies decrease with increasing cluster size as exposed Pt atoms become more coordinatively saturated (Table 2), as expected from bond-order conservation principles, which preserve the total bond order (O–Pt and Pt–Pt bonds) and bond energy for each Pt atom.⁹⁸ Weakly chemisorbed O^* atoms predominantly present on larger Pt clusters form stronger bonds with the H atoms at the transition state, thus decreasing activation barriers ($E_{1[\text{O}^*\text{--O}^*]}$) and increasing C–H bond activation rate constants ($k_{1[\text{O}^*\text{--O}^*]}$).

In regime 2, both the C–H and $\text{O}=\text{O}$ bond activation steps are kinetically relevant. The weakly bound O^* atoms prevalent on larger Pt clusters are more effective for H abstraction, as shown from the linear decrease in C–H bond activation barriers with O^* binding energies calculated from DFT (section 3.3; Figure S-3 in the Supporting Information). The weaker O^* binding strengths also infer less effective O_2 dissociation steps, as predicted from the BEP relationship between the O_2 dissociation barriers and the exothermicity of the reactions (also related to the heats of O^* adsorption). These weaker O^* bindings lead to higher C–H bond activation and lower $\text{O}=\text{O}$ bond dissociation rate

Table 3. Effects of Average Pt Cluster Size on Rate Constants for the Various Kinetic Regimes During $\text{CH}_4\text{--O}_2$ Reactions on 0.2% wt Pt/ Al_2O_3 Catalysts at 873 K^a

average Pt cluster size (nm)	kinetic regimes and effective rate constants ($\text{kPa}^{-1} \text{s}^{-1}$)			
	1 $k_{1[\text{O}^*\text{--O}^*]}$	2 $2k_{1[\text{O}^*\text{--}]}(k_{2\text{bf}}K_{2\text{a}})^{-1}$	3 $0.5k_{2\text{bf}}K_{2\text{a}}$	4 (reforming) ^b $k_{1[*\text{--}]}^b$
1.8 nm cluster ^c	0.44	5.7	2164	1.2
3.3 nm cluster ^c	0.58	9.7	2520	0.88
8.5 nm cluster	1.1	22	2800	0.53

^a 0.15 mg cat., 200 SiO_2 /catalyst intraparticle (λ) and 4700 quartz/catalyst interparticle (χ) dilution ratios, 2.08 cm^3 (STP) s^{-1} . ^b from ref 7. ^c Initial rate constants.¹⁰¹

constants and, in turn, to larger effective rate constants ($k_{\text{app},2} = 2k_{1[\text{O}^*\text{--}]}^2(k_{2\text{bf}}K_{2\text{a}})^{-1}$) on the larger Pt clusters. These effects on rates are, however, partly compensated by an increase in C–H bond activation barriers caused by weaker interactions between the oxygen vacancy sites ($*$) and the CH_3 in the $(*\text{--CH}_3\text{--H--O}^*)^\ddagger$ transition state (section 3.3). As a result, effective rate constants depend weakly on cluster size and vary only by a factor of < 4 between the 1.8 and 8.5 nm Pt clusters, even though they reflect the square of the C–H bond activation rate constant ($k_{1[\text{O}^*\text{--}]}^2$).

Isotopic $^{16}\text{O}_2\text{--}^{18}\text{O}_2$ exchange rates confirm that O^* binding strength increases with decreasing Pt cluster size. $^{16}\text{O}_2\text{--}^{18}\text{O}_2$ exchange rate constants on 8.5 nm Pt clusters are ~ 2.5 times larger than on 1.8 nm clusters at 873 K (Figure 5). These rate constants (eq 6b) depend on the ratio of O_2^* and O^* equilibrium adsorption constants ($K_{2\text{a}}$ and $K_{2\text{b}}$, respectively) and the $^{16}\text{O}^*$ and $^{18}\text{O}_2^*$ (or $^{18}\text{O}^*$ and $^{16}\text{O}_2^*$) reaction rate constants (k_{11} , Step 11). The effective barrier for $^{16}\text{O}_2\text{--}^{18}\text{O}_2$ reactions ($E_{\text{ex,app}}$) depends on the heats of molecular ($Q_{2\text{a}}$) and atomic ($Q_{2\text{b}}$) oxygen adsorption⁹⁹ and on the activation barrier ($E_{11\text{f}}$) for the $^{16}\text{O}^*$ and $^{18}\text{O}_2^*$ (or $^{18}\text{O}^*$ and $^{16}\text{O}_2^*$) exchange step

$$E_{\text{ex,app}} = E_{11\text{f}} + 0.5(Q_{2\text{b}} - Q_{2\text{a}}) \quad (23)$$

The $(Q_{2\text{b}} - Q_{2\text{a}})$ term is positive because the heat of O^* adsorption ($Q_{2\text{b}}$, $171.5 \text{ kJ mol}^{-1}$) is much larger than the heat of molecular O_2 adsorption ($Q_{2\text{a}}$, 15.9 kJ mol^{-1}), as established previously from thermal desorption experiments on Pt(111) surfaces,^{93,100} and consistent with DFT results in Figure 10 on both the bare and O^* covered Pt clusters. The larger O_2 exchange rate constants on the 8.5 nm clusters could reflect lower apparent activation barriers, as a result of the weaker O^* binding ($Q_{2\text{b}}$) and/or smaller differences between the heats of atomic and molecular oxygen adsorption ($Q_{2\text{b}} - Q_{2\text{a}}$). It is expected that the barriers for $^{16}\text{O}^*$ and $^{18}\text{O}_2^*$ exchange may also be affected by the cluster size but to a lesser extent because energy stabilizations of reactant and product states are affected by the O^* binding strength to a similar extent.

Finally, the slope of the $r_{\text{CH}_4}(\text{CH}_4)^{-1}$ versus O_2/CH_4 data in regime 3 (Figure 14, $\text{O}_2/\text{CH}_4 < 0.02$ for 1.8 to 8.5 nm Pt clusters; Table 3) reflects the rate constants of O_2 activation on uncovered Pt surfaces ($0.5K_{2\text{a}}k_{2\text{bf}}$, eq 20). The effective rate constants, unlike those for other regimes, depend strictly on the sticking coefficients of O_2 and remain insensitive to cluster size (1.8–8.5 nm) because O_2 dissociation is a nonactivated step ($\sim 3 \text{ kJ mol}^{-1}$; Table 1).

Cluster size effects on reactive CH_4 collision probabilities ($r_{\text{CH}_4}(\text{CH}_4)^{-1}$), as expected, differ in each kinetic regime. The reactive CH_4 collision probabilities may increase (regimes 1 and 2), decrease (regime 4), or remain unchanged (regime 3) with increasing cluster sizes and surface Pt coordination, because they reflect different elementary rate constants depending on the identity of the kinetically relevant step and the involvement of Pt atoms and oxygen vacancies.

3.7. Fundamental Relations between First-Order Rate Constants and O_2/CH_4 Ratios and Oxygen Coverages and the Limits of Langmuirian Treatments of Surface Reactions. The seemingly complex kinetic behavior of catalytic $\text{CH}_4\text{--O}_2$ reactions on Pt clusters and the observed transitions among kinetic regimes depend on either the O_2 pressures (regime 1) or prevalent O_2/CH_4 ratios (regimes 2 and 3), because these parameters set the oxygen chemical potentials (also the oxygen virtual pressures) at catalytic surfaces and, in turn, the O^* coverages during steady-state catalysis. CH_4 molecules colliding with Pt cluster surfaces encounter a distribution of $\text{O}^*\text{--O}^*$, $\text{O}^*\text{--}^*$, and $^*\text{--}^*$ site pairs. The reactivity and rate equation in each regime (shown as the first-order rate constant $r_{\text{CH}_4}(\text{CH}_4)^{-1}$ in Figures 3 and 14) reflect the predominance of a specific activating site pair and the identity of the respective kinetically relevant step through the defining role of O^* coverages and oxygen virtual pressures.

At O_2/CH_4 ratios above 2 (regime 1), $\text{O}^*\text{--O}^*$ pairs prevalent on O^* -saturated clusters activate C–H bonds in CH_4 reactants; O^* coverages are unaffected by O_2 pressures at O^* saturation and $r_{\text{CH}_4}(\text{CH}_4)^{-1}$ become true rate constants that reflect the CH_4 reactive probabilities upon collisions with cluster surfaces. Oxygen vacancies (exposed Pt atoms) emerge at O_2/CH_4 ratios lower than 2 (regime 2) and $\text{O}^*\text{--}^*$ site pairs provide a more effective parallel C–H bond activation route. The number of * sites is set by the kinetic coupling between the steps that form them (C–H activation) and consume them (O_2 activation) and therefore by O_2/CH_4 ratios (eqs 18a and 18b). The $r_{\text{CH}_4}(\text{CH}_4)^{-1}$ values are no longer constant but instead become inversely proportional to O_2/CH_4 ratios. At O_2/CH_4 ratios near the point of O_2 depletion (<0.08 , regime 3), rates become limited by O_2 activation and proportional to O_2 pressure, causing rate constants ($r_{\text{CH}_4}(\text{CH}_4)^{-1}$) to increase linearly with O_2/CH_4 ratios.

These rate equations are based on noninteracting O^* and * species and elementary rate and equilibrium constants that do not depend on O^* coverages, an assumption that becomes rigorous at the extremes of bare (regimes 3 and 4) and O^* -saturated (regime 1) cluster surfaces. Such assumptions also seem appropriate near the transition between regimes 1 and 2, for which vacancies are isolated minority species on Pt cluster surfaces nearly saturated with O^* atoms. As the system approaches the transition between regimes 2 and 3, the rate and equilibrium constants and the binding energy and reactivity of O^* species are expected to vary with O^* coverage, causing deviations from the kinetic behavior derived based on Langmuirian assumptions. These considerations are borne out by the deviations between the predictions from eq 11 for regime 2 and the data shown in Figure 7 near the transition between regimes 2 and 3 ($\text{CH}_4/\text{O}_2 > 8$). These effects reflect the formation of diverse structures in which the number of vicinal vacancies differs, leading to concomitant changes in the binding energy of CH_3 fragments on exposed metals and in the binding energy and reactivity of O^* . These subtle transitions between surfaces that cannot be rigorously treated as Langmuirian ensembles require

the adoption of more realistic DFT-based theoretical descriptions combined with kinetic Monte Carlo simulations. We have carried out these simulations using DFT-derived rate and equilibrium parameters on model Pt(111) surfaces, as will be described in detail elsewhere.

4. CONCLUSIONS

A simple sequence of elementary reaction steps and their kinetic relevance are established based on kinetic dependencies, CH_4/CD_4 kinetic isotope effects, isotopic exchange evidence, and density functional theory results to describe the seemingly complex reaction kinetics observed during CH_4 reactions with O_2 , H_2O , or CO_2 oxidants on supported Pt clusters. Four kinetic regimes, each with a unique rate equation and kinetic dependence, are detected. These regimes reflect the changes in the identities of kinetically relevant step and active site structure as O^* coverages decrease from saturation to uncovered. C–H bond activation is kinetically relevant in three of the four regimes but proceeds via mechanistically different paths on $\text{O}^*\text{--O}^*$, $\text{O}^*\text{--}^*$, or $^*\text{--}^*$ site pairs, the relative abundances of which depend on O^* coverages. In a narrow regime before the complete O_2 depletion, C–H bond activation becomes kinetically irrelevant and O_2 activation on uncovered Pt clusters limits the CH_4 conversion rates.

C–H bond activation on $\text{O}^*\text{--O}^*$ site pairs proceeds via an O^* assisted hydrogen abstraction route that involves the formation of a radical-like CH_3 transition state complex, characterized by low entropy losses and high activation barriers. In contrast, C–H bond activation on Pt atom site pairs ($^*\text{--}^*$) proceeds via an oxidative addition route in which one of the Pt atoms inserts into the C–H bond, forming a three-centered Pt–C–H transition state. Similar oxidative addition route occurs during C–H bond activation on $\text{O}^*\text{--}^*$ site pairs, but assisted by O^* , which polarizes the C–H bond and abstracts the H. The barriers for C–H bond activation on $\text{O}^*\text{--O}^*$ and $\text{O}^*\text{--}^*$ site pairs are correlated to the reactivity of O^* in H abstraction and thus to the oxygen binding strengths. The barriers for C–H bond activation on $\text{O}^*\text{--}^*$ site pairs are also influenced by the binding strength of CH_3 on the oxygen vacancy site, as also found for similar steps on $^*\text{--}^*$ site pairs, because both of these steps involve the oxidative addition of Pt atoms into the C–H bond.

Reactive CH_4 collision probabilities (also the pseudo first-order rate constants, $r_{\text{CH}_4}(\text{CH}_4)^{-1}$) are a single-value function of O_2/CH_4 ratios because they either (i) are insensitive to O_2/CH_4 ratios on surfaces saturated with or uncovered of O^* or (ii) depend strictly on O_2/CH_4 ratios that set the O^* coverages on Pt surfaces. The Pt cluster size and, specifically, Pt coordination number and O^* binding strength influence rates differently in each of these regimes depending on the associated kinetically relevant steps. First-order rate constants are higher on larger Pt clusters when O^* atoms are involved in C–H bond activation (i.e., on $\text{O}^*\text{--O}^*$ and $\text{O}^*\text{--}^*$ site pairs), because weakly bound O^* atoms prevalent on larger clusters are more effective for hydrogen abstraction than those on smaller clusters. The opposite trend was found for C–H bond activation on $^*\text{--}^*$ site pairs, because coordinatively less saturated Pt atoms prevalent on small clusters form stronger metal–carbon bonds with CH_3 , increasing the reaction exothermicity and thus lowering the barriers. In contrast, CH_4 turnover rates are insensitive to cluster sizes when O_2 dissociation controls rates, because this step is nonactivated and determined strictly by the O_2 collision rates.

The diversity of rate dependencies, activation enthalpies and entropies, and cluster size effects in CH₄–O₂ reactions on Pt surfaces are rigorously described by a shift in the identity of kinetically relevant steps and active site structures in response to changes in oxygen coverages and their reactivities that are set by the oxygen virtual pressures at catalytic surfaces.

■ ASSOCIATED CONTENT

S Supporting Information. Derivation of CH₄ reaction rates limited by C–H bond activation on O*–O* site pairs on Pt surfaces; derivation of isotopic ¹⁶O₂–¹⁸O₂ exchange rate expression; structures of reactant, transition state, and product for the initial C–H bond dissociation in CH₄ over O*–O* site pairs on Pt₂₀₁ clusters saturated with chemisorbed oxygen atoms; derivation of the CH₄ turnover rate equation with the assumptions that irreversible C–H bond activation on O*–O* site pairs is the kinetically relevant step; structures of (H₃C*–OH)[‡] transition state complexes during C–H bond dissociation on O*–O* site pairs; effects of O* binding strength on the barriers of C–H bond activation on O*–O* site pairs. This material is available free of charge via the Internet at <http://pubs.acs.org>.

■ AUTHOR INFORMATION

Corresponding Author

iglesia@berkeley.edu (E. Iglesia); mn4n@virginia.edu (M. Neurock)

■ ACKNOWLEDGMENT

This study was supported by BP as part of the Methane Conversion Cooperative Research Program at the University of California at Berkeley and at the University of Virginia. We also gratefully acknowledge the computational support from the Molecular Science Computing Facility (MSCF) in the William R. Wiley Environmental Molecular Sciences Laboratory, a national scientific user facility sponsored by the U.S. Department of Energy's Office of Biological and Environmental Research and located at the Pacific Northwest National Laboratory. Pacific Northwest is operated for the Department of Energy by Battelle.

■ REFERENCES

- (1) Twigg, M. V. *Catalyst Handbook*, 2nd ed.; Manson: London, 1994.
- (2) Rostrup-Nielsen, J. R. *Catal. Today* **1993**, *18*, 305.
- (3) Rostrup-Nielsen, J. R.; Sehested, J. *Adv. Catal.* **2002**, *47*, 65.
- (4) Rostrup-Nielsen, J. R. Catalytic Steam Reforming. In *Catalysis Science and Technology*; Andersen, J. R., Boudart, M., Eds.; Springer: Berlin, 1984; Vol 5, p 1.
- (5) Wei, J. M.; Iglesia, E. *J. Catal.* **2004**, *224*, 370.
- (6) Wei, J. M.; Iglesia, E. *J. Catal.* **2004**, *225*, 116.
- (7) Wei, J. M.; Iglesia, E. *J. Phys. Chem. B* **2004**, *108*, 4094–4103.
- (8) Wei, J. M.; Iglesia, E. *Angew. Chem., Int. Ed.* **2004**, *43*, 3685.
- (9) Wei, J. M.; Iglesia, E. *Phys. Chem. Chem. Phys.* **2004**, *6*, 3754.
- (10) Wei, J. M.; Iglesia, E. *J. Phys. Chem. B* **2004**, *108*, 7253.
- (11) Yamaguchi, A.; Iglesia, E. *J. Catal.* **2010**, *274*, 52.
- (12) Ashcroft, A. T.; Cheetham, A. K.; Green, M. L. H.; Vernon, P. D. F. *Nature* **1991**, *352*, 225.
- (13) Prettre, M.; Eichner, C.; Perrin, M. *Trans. Faraday Soc.* **1946**, *42*, 335.
- (14) Vernon, P. D. F.; Green, M. L. H.; Cheetham, A. K.; Ashcroft, A. T. *Catal. Lett.* **1990**, *6*, 181.
- (15) Ashcroft, A. T.; Cheetham, A. K.; Foord, J. S.; Green, M. L. H.; Grey, C. P.; Murrell, A. J.; Vernon, P. D. F. *Nature* **1990**, *344*, 319.
- (16) Aasberg-Petersen, K.; Hansen, J. H. B.; Christensen, T. S.; Dybkjaer, I.; Christensen, P. S.; Nielsen, C. S.; Madsen, S.; Rostrup-Nielsen, J. R. *Appl. Catal., A* **2001**, *221*, 379.
- (17) Hickman, D. A.; Schmidt, L. D. *Science* **1993**, *259*, 343.
- (18) Hickman, D. A.; Haupfear, E. A.; Schmidt, L. D. *Catal. Lett.* **1993**, *17*, 223.
- (19) Mhadeshwar, A. B.; Vlachos, D. G. *Ind. Eng. Chem. Res.* **2007**, *46*, 5310.
- (20) O'Connor, A. M.; Ross, J. R. H. *Catal. Today* **1998**, *46*, 203.
- (21) Heitnes, K.; Lindberg, S.; Rokstad, O. A.; Holmen, A. *Catal. Today* **1995**, *24*, 211.
- (22) van Looij, F.; Stobbe, E. R.; Geus, J. W. *Catal. Lett.* **1998**, *50*, 59.
- (23) Dissanayake, D.; Rosynek, M. P.; Kharas, K. C. C.; Lunsford, J. H. *J. Catal.* **1991**, *132*, 117.
- (24) Beretta, A.; Gianpiero, G.; Lualdi, M.; Tavazzi, I.; Forzatti, P. *Ind. Eng. Chem. Res.* **2009**, *48*, 3825.
- (25) Enger, B. C.; Lødeng, R.; Holmen, A. *Appl. Catal.* **2008**, *346*, 1.
- (26) Chin, Y.-H.; Buda, C.; Neurock, M.; Iglesia, E. *J. Catal.* in press, doi:10.1016/j.jcat.2011.06.011.
- (27) Chin, Y.-H.; Iglesia, E. *J. Phys. Chem. C* in press, doi: 10.1021/jp203324y.
- (28) David, R. L. *Handbook of Chemistry and Physics*, 87th ed.; CRC Press: Boca Raton, FL, 2006; pp 4–81.
- (29) Abild-Pedersen, F.; Lytken, O.; Engbaek, J.; Nielsen, G.; Chorkendorff, I.; Norskov, J. K. *Surf. Sci.* **2005**, *590* (2–3), 127.
- (30) Anghel, A. T.; Wales, D. J.; Jenkins, S. J.; King, D. A. *Phys. Rev. B* **2005**, *71*, 11.
- (31) Bunnik, B. S.; Kramer, G. J. *J. Catal.* **2006**, *242* (2), 309.
- (32) Burghgraef, H.; Jansen, A. P. J.; van Santen, R. A. *Surf. Sci.* **1995**, *324* (2–3), 345.
- (33) Ciobica, I. M.; Frechard, F.; van Santen, R. A.; Kleyn, A. W.; Hafner, J. A. *J. Phys. Chem. B* **2000**, *104* (14), 3364.
- (34) Henkelman, G.; Jonsson, H. *Phys. Rev. Lett.* **2001**, *86* (4), 664.
- (35) Jones, G.; Jakobsen, J. G.; Shim, S. S.; Kleis, J.; Andersson, M. P.; Rossmeisl, J.; Abild-Pedersen, F.; Bligaard, T.; Helveg, S.; Hinnemann, B.; Rostrup-Nielsen, J. R.; Chorkendorff, I.; Sehested, J.; Norskov, J. K. *J. Catal.* **2008**, *259* (1), 147.
- (36) Kokalj, A.; Bonini, N.; Sbraccia, C.; de Gironcoli, S.; Baroni, S. *J. Am. Chem. Soc.* **2004**, *126* (51), 16732.
- (37) Kokalj, A.; Bonini, N.; de Gironcoli, S.; Sbraccia, C.; Fratesi, G.; Baroni, S. *J. Am. Chem. Soc.* **2006**, *128* (38), 12448.
- (38) Pallassana, V.; Neurock, M. *J. Catal.* **2000**, *191* (2), 301.
- (39) Petersen, M. A.; Jenkins, S. J.; King, D. A. *J. Phys. Chem. B* **2004**, *108* (19), 5909.
- (40) Vines, F.; Lykhach, Y.; Staudt, T.; Lorenz, M. P. A.; Papp, C.; Steinruck, H. P.; Libuda, J.; Neyman, K. M.; Gorling, A. *Chem.—Eur. J.* **2010**, *16* (22), 6530.
- (41) Weaver, J. F.; Hakanoglu, C.; Hawkins, J. M.; Asthagiri, A. *J. Chem. Phys.* **2010**, *132* (2), 024709.
- (42) Zhang, C. J.; Hu, P. *J. Chem. Phys.* **2002**, *116* (1), 322.
- (43) Fratesi, G.; Gava, P.; de Gironcoli, S. *J. Phys. Chem. C* **2007**, *111*, 17015.
- (44) Ishikawa, A.; Neurock, M.; Iglesia, E. *J. Am. Chem. Soc.* **2007**, *129*, 13201.
- (45) Kresse, G.; Hafner, J. *Phys. Rev. B* **1994**, *49*, 14251.
- (46) Kresse, G.; Furthmüller, J. *Comput. Mater. Sci.* **1996**, *6*, 15.
- (47) Kresse, G.; Furthmüller, J. *Phys. Rev. B* **1996**, *54*, 11169.
- (48) Perdew, J. P.; Chevary, J. A.; Vosko, S. H.; Jackson, K. A.; Pederson, M. R.; Singh, D. J.; Fiolhais, C. *Phys. Rev. B* **1992**, *46*, 6671.
- (49) Vanderbilt, D. *Phys. Rev. B* **1990**, *41*, 7892.
- (50) Van Harveld, R.; Hartog, F. *Surf. Sci.* **1969**, *15*, 189.
- (51) Monkhorst, H. J.; Pack, J. D. *Phys. Rev. B* **1976**, *13*, 5188.
- (52) Henkelman, G.; Uberuaga, B. P.; Jonsson, H. *J. Chem. Phys.* **2000**, *113*, 9901.
- (53) Henkelman, G.; Jonsson, H. *J. Chem. Phys.* **2000**, *113*, 9978.
- (54) Sheppard, D.; Terrell, R.; Henkelman, G. *J. Chem. Phys.* **2008**, *128*, 134106.

- (55) The CH₄-CD₄ cross exchange rates were calculated from the sum of CH₃D, CHD₃, and two times the CH₂D₂ concentrations. The CH₄-CD₄ exchange rates from Al₂O₃ supports were comparable to those on Pt clusters for the 0.2% wt. Pt/Al₂O₃ catalyst. SiO₂ support, however, gives negligible CH₄-CD₄ exchange rates. CH₄-CD₄ exchange rates during CH₄-CD₄-O₂ were measured on a 0.2% wt Pt/SiO₂ catalyst to eliminate contribution from the support.
- (56) Boudart, M. *J. Phys. Chem.* **1983**, *87*, 2786.
- (57) Kemball, C. *Discuss. Faraday Soc.* **1966**, *41*, 190.
- (58) Boudart, M. *Catal. Lett.* **1989**, *3*, 111.
- (59) Temkin, M.; Pyzhez V. *Zhur. Fiz. Khim.* **1939**, *13*, 851.
- (60) Yu, S. Y.; Biscardi, J. A.; Iglesia, E. *J. Phys. Chem. B* **2002**, *106*, 9642.
- (61) Weiss, B. M.; Iglesia, E. *J. Phys. Chem. C* **2009**, *113*, 13331.
- (62) Muller, O.; Roy, R. *J. Less-Common Metals* **1968**, *16*, 129.
- (63) McCarty, J. G. *Catal. Today* **1995**, *26*, 283.
- (64) Chin Y.-H.; Buda C.; Neurock, M.; Iglesia, E., in preparation.
- (65) Li, H. Y.; Guo, Y. L.; Lu, G.; Hu, P. *J. Chem. Phys.* **2008**, *128*, 051101.
- (66) Weaver, J.; Hinojosa, J. A.; Hakanoglu, C.; Antony, A.; Hawkins, J. M.; Asthagiri, A. *Catal. Today* **2011**, *160*, 213.
- (67) Weaver, J. F.; Chen, J. J.; Gerrard, A. L. *Surf. Sci.* **2005**, *592*, 83.
- (68) Chin, Y.-H.; Iglesia, E. unpublished results.
- (69) Eichler, A.; Mittendorfer, F.; Hafner, J. *Phys. Rev. B* **2000**, *62*, 4755.
- (70) Tang, H. R.; Van der Ven, A.; Trout, B. L. *Phys. Rev. B* **2004**, *70*, 045420.
- (71) Legare, P. *Surf. Sci.* **2005**, *580*, 137.
- (72) Getman, R. B.; Xu, Y.; Schneider, W. F. *J. Phys. Chem. C* **2008**, *112*, 9559.
- (73) Benson, J. E.; Boudart, M. *J. Catal.* **1965**, *4*, 704.
- (74) Pre-exponential factor is estimated using transition state theory treatment on the C-H bond activation step by assuming that the CH₄(g) reactant forms a mobile transition state complex, which retains two translational degrees of freedom. It is assumed that the contributions from the rotational and vibrational partition functions on the pre-exponential factors are unimportant compared to that of translational partition functions.
- (75) Buda C.; Neurock, M. 2009, unpublished results.
- (76) Rozanska, X.; Kondratenko, E. V.; Sauer, J. *J. Catal.* **2008**, *256*, 84.
- (77) Lunsford, J. H. *Angew. Chem., Int. Ed.* **1995**, *34*, 970.
- (78) Fujimoto, K.; Ribeiro, F. H.; Avalos-Borja, M.; Iglesia, E. *J. Catal.* **1998**, *179*, 431.
- (79) García-Diéguez, M.; Chin Y.-H.; Iglesia, E. *J. Catal.*, submitted.
- (80) Although O* atoms are not involved in the C-H bond activation on *-* site pairs, they are consumed later along the reaction coordinate in kinetically irrelevant O* insertion steps at rates that are equal to the kinetically relevant C-H bond activation on *-* site pairs.
- (81) The forward CH₄ turnover rates are equal to the net rates of O₂ dissociation, $2k_{1[O^*]}(CH_4)(O^*)(*) = k_{2bf}(O_2)(*)^2 - k_{2br}(O^*)^2$.
- (82) Crabtree, R. H. *The Organometallic Chemistry of Transition Metals*; J. Wiley and Sons, 1994.
- (83) Cundari, T. R.; Grimes, T. V.; Gunnoe, T. B. *J. Am. Chem. Soc.* **2007**, *129*, 13172.
- (84) Cummins, C. C.; Baxter, S. M.; Wolczanski, P. T. *J. Am. Chem. Soc.* **1988**, *110*, 8731.
- (85) Cummins, C. C.; Schaller, C. P.; Van Duyne, G. D.; Wolczanski, P. T.; Chan, A. W. E.; Hoffmann, R. *J. Am. Chem. Soc.* **1991**, *113*, 2985.
- (86) The O* binding strength is defined as the energy required to remove an O* from the O* covered Pt(111) surfaces, also the absolute values of the reaction energies for the $nO^*/Pt(111) \rightarrow (n-1)O^*/Pt(111) + O$ reactions.
- (87) Madix, R. J.; Roberts, J. T. The Problem of Heterogeneously Catalyzed Partial Oxidation: Model Studies on Single Crystal Surfaces. In *Surface Reactions*, Madix, R. J., Ed.; Springer-Verlag: Berlin, 1994; pp 5–53.
- (88) van Santen, R. A.; Neurock, M.; Shetty, S. G. *Chem. Rev.* **2010**, *110*, 2005.
- (89) Wasileski, S. A.; Janik, M. J.; Plaisance, C. P.; Van Santen, R. A.; Neurock, M. A First Principles Analysis of Periodic Trends in the C-H and O-H Activation over Closed Packed Transition Metal Surfaces. *J. Phys. Chem. C*, to be submitted.
- (90) Weiss, B. M.; Iglesia, E. *J. Catal.* **2010**, *272*, 74.
- (91) Devarajan, S. P.; Hinojosa, J. A.; Weaver, J. F. *Surf. Sci.* **2008**, *602*, 3116.
- (92) Bonini, N.; Kokalj, A.; Dal Corso, A.; de Gironcoli, S.; Baroni, S. *Phys. Rev. B* **2004**, *69*, 195401.
- (93) Campbell, C. T.; Ertl, G.; Kuipers, H.; Segner, J. *Surf. Sci.* **1981**, *107*, 220.
- (94) Dumesic, J. A.; Rudd, D. R.; Aparicio, L. M.; Rekoske, J. E.; Trevino, A. A. *The Microkinetics of Heterogeneous Catalysis*; ACS Professional Reference Book; American Chemical Society: Washington, DC, 1993; p 40.
- (95) Allian, A. D.; Takanebe, K.; Fudjald, K. L.; Hao, X.; Truex, T. J.; Cai, J.; Buda, C.; Neurock, M.; Iglesia, E. *J. Am. Chem. Soc.* **2011**, *133* (12), 4498.
- (96) Shan, B.; Zhao, Y.; Hyun, J.; Kapur, N.; Nicholas, J. B.; Cho, K. *J. Phys. Chem. C* **2009**, *113*, 6088.
- (97) Eichler, A.; Hafner, J. *Phys. Rev. Lett.* **1997**, *79*, 4481.
- (98) Benziger, J. Thermochemical Methods for Reaction Energetics on Metal Surfaces. In *Metal-Surface Reaction Energetics: Theory and Applications to Heterogeneous Catalysis, Chemisorption, and Surface Diffusion*, Shustorovich, E., Ed.; VCH: Weinheim, 1991; pp 53–107.
- (99) Q_{2a} and Q_{2b} are equal to $-\Delta H_{2a}$ and $-\Delta H_{2b}$, the reaction enthalpies for Steps 2.1 and 2.2 in Scheme 2, respectively.
- (100) Gland, J. L. *Surf. Sci.* **1980**, *93*, 487.
- (101) For the smaller Pt clusters (1.8 and 3.3 nm average diameters), the rate constants for regimes 1–3 decreased with the reaction time-on-stream. We rule out metal sintering as the cause of the activity decrease because these samples have been treated to higher temperatures (>898 K). Similar trends were also detected for supported Pd clusters, as will be reported in a separate contribution (ref 27).